

## Relative timing of substorm processes as derived from multifluid/multiscale simulations: Internally driven substorms

R. M. Winglee,<sup>1</sup> E. Harnett,<sup>1</sup> and A. Kidder<sup>1</sup>

Received 12 September 2008; revised 8 June 2009; accepted 22 June 2009; published 24 September 2009.

[1] The role of tail reconnection in initiating substorm onset remains highly controversial. Multifluid/multiscale simulations are used to examine this problem with the unique capability of being able to resolve ion skin depth and ion cyclotron processes within a very thin tail current sheet within a global magnetosphere. It is shown that, consistent with the near-Earth neutral line model, a thin current sheet forms during the growth phase with the eventual formation of an X line and the ejection of a plasmoid. However, these processes do not produce substorm onset but are precursors to onset. The modeling indicates that in the wake of the plasmoid, a Y line forms within which there is the intermittent generation of flux ropes that can propagate either earthward or tailward with equal probability. The intensity and size of the flux ropes are seen to increase in time up to substorm onset. Depending on the size of the earthward moving flux rope, pseudobreakup or substorm onset occurs when the energy within the earthward moving flux rope is dissipated against the inner edge of the plasma sheet. This interaction leads to rapid (1 min) dipolarization, magnetospheric injection of energetic particles, and intensification of the nightside auroral currents that expand in local time and to higher latitudes. These processes are consistent with the current disruption model where onset occurs as a direct consequence of processes occurring at the inner edge of the plasma sheet. Ionospheric outflows and their energization with the thin current sheet play important roles in the buildup of energy in the plasma sheet that eventually produces substorm onset and drives breakup.

**Citation:** Winglee, R. M., E. Harnett, and A. Kidder (2009), Relative timing of substorm processes as derived from multifluid/multiscale simulations: Internally driven substorms, *J. Geophys. Res.*, 114, A09213, doi:10.1029/2008JA013750.

### 1. Introduction

[2] A comprehensive model for the development of substorms is one of the outstanding problems of space physics. The sequence of events that comprise a substorm from the auroral viewpoint is well documented [Akasofu, 1964; McPherron, 1970]. Substorms consist of three phases. First, in the growth phase the polar cap, which is enclosed by the auroral oval, is seen to expand toward lower latitudes in association with the stretching of the nightside field lines. The second phase is onset which is associated with a sudden brightening of the equatorward arc, and dipolarization of the magnetic field. Onset is called “breakup” only if there is rapid (on a time scale of 0–5 min) poleward and azimuthal expansion of auroral arcs. If there is only limited poleward and azimuthal expansion then the term “pseudobreakup” is used [Meng and Liou, 2004]. The last phase or recovery phase sees the return of the auroral oval to a brightness and position associated with quiet conditions.

[3] The corresponding features that occur in the magnetosphere are more controversial. The two main mechanisms

are (1) the near-Earth neutral line model (NENL) [Hones, 1984; Baker *et al.*, 1996] where substantial thinning of the plasma sheet in the tail eventually leads to the formation of a magnetic X line (or magnetic null) at 15–25  $R_E$  (Earth radii) producing strong acceleration of the plasma both toward the Earth and down the magnetotail and (2) the current disruption (CD) model [Lui *et al.*, 1992; Lui, 1996] where plasma instabilities lead to the disruption of the inner plasma sheet (at  $<10 R_E$ ) causing the energization of the plasma in association with the magnetic fields lines becoming more dipole-like (dipolarization).

[4] The strength of the NENL model is that reconnection signatures in the tail have been confirmed observationally [Slavin *et al.*, 1989; Moldwin and Hughes, 1992], and is a central feature of existing global magnetospheric models [Ogino, 1986; Slinker *et al.*, 1995]. The weakness of the NENL model is that the auroral oval is predicted to expand from high to low latitudes, contrary to observations, and there is evidence that the energy release occurs at 6–10  $R_E$  [Feldstein and Galperin, 1985; Lopez *et al.*, 1990; Lui, 1991; McIlwain, 1992; Kennel, 1992]. The strength of the CD model is that the initiation of the substorm occurs near the inner edge of the plasma sheet so that the auroral oval at onset expands poleward, starting near the equatorward edge of the auroral oval [Lui, 2004]. The weakness lies in tying

<sup>1</sup>Department of Earth and Space Sciences, University of Washington, Seattle, Washington, USA.

the suggested dynamics to commonly observed processes in the near-Earth magnetotail.

[5] The present constellation of Earth-observing spacecraft has allowed detailed examination of the tail dynamics relative to substorm onset as determined by ultraviolet (UV) imaging of the global aurora. One example by *Baker et al.* [2002] used data from the Wideband Imaging Camera (WIC) on the IMAGE spacecraft to compare the timing on substorm onset relative to the development of reconnection observed by Cluster. *Baker et al.* [2002] concluded that the processes causing the auroral breakup occurs at  $\sim 8 R_E$ , with in situ observations from Cluster showing reconnection processes at  $18 R_E$  down the tail. *Baker et al.* [2002] noted that the reconnection occurred about 7 min prior to the observed onset and that magnetic reconnection process is the causative driver of dissipation for substorm onset. *Meng and Liou* [2004] indicated there is a problem with this type of conclusion, in that the fast flows from such reconnection should only take 1–2 min to arrive at the inner edge of the plasma sheet; shorter than the observed time delay of 7 min.

[6] Recent results from the Time History of Events and Macroscale Interactions During Substorms (THEMIS) mission confirm that reconnection occurs before substorm onset. In their case onset is determined by a ground station magnetometer data and reconnection is observed by the spacecraft at  $\sim 20 R_E$  [*Angelopoulos et al.*, 2008]. Because the reconnection is inferred to have occurred 1.5 min before substorm onset, they conclude that reconnection initiates substorm onset, consistent with the NENL model.

[7] A different analysis of a large number of substorm events by *Liou et al.* [2002] yielded a very different conclusion. *Liou et al.* studied 32 unambiguous dipolarization events (determined from GOES 8 and GOES 9) that had ionospheric footprints within 2 h of magnetic local time (MLT), from their associated auroral breakups identified from Polar UVI observations. Their results indicated that auroral breakup preceded the arrival of dipolarization at GOES by an average of  $1.7 \pm 2.7$  min, with a delay attributable to a propagation time. The propagation speed was estimated to be about 60–70 km/s in the east-west direction, and about 270 km/s toward the earth. The timing indicated that the source of the dipolarization was within  $1 R_E$  of the geosynchronous spacecraft, suggesting that reconnection is not the cause of substorm onset.

[8] Not only is there substantial debate about whether the NENL or CD models can account for substorm onset, but there is also significant discussion as to whether substorms are triggered internally or externally. *Lyons et al.* [1997] examined 20 substorms that were well observed by the Canadian Auroral Network for the OPEN Program United Study (CANOPUS). They found that 14 of the 20 substorms had a clear external trigger in the form of a northward turning or a reduction in the magnitude of the  $y$  component of the interplanetary magnetic field (IMF). All but one of the identified triggers was associated with northward turnings. They also noted that substorm onset occurred approximately 9 min after the arrival of the northward turning at the magnetopause, and that typically 60–70 min was the median time period for southward IMF driving the triggered substorm. The fact that not all the substorms appeared to be triggered is consistent with earlier observations that sub-

storms can occur under stable solar wind and IMF conditions [*Horwitz*, 1985; *Henderson et al.*, 1996].

[9] An additional problem with the NENL model is that its initial concept of how reconnection occurs in the magnetotail is too simple. The early NENL models showed a well-defined O-type neutral line within plasmoids [*Hones*, 1984]. Subsequent studies have shown that in addition to plasmoids, smaller-scale flux ropes can occur with the negative  $B_z$  signature of plasmoids but with an appreciable core magnetic field [*Sibeck et al.*, 1984; *Elphic et al.*, 1986; *Slavin et al.*, 1989; *Sibeck et al.*, 1990; *Moldwin and Hughes*, 1991, 1992]. On occasion, the core magnetic field can be as strong as, and in some cases exceed, the lobe magnetic field [*Slavin et al.*, 1995]. *Lepping et al.* [1995, 1996] used a force-free model for flux ropes to show that in both the midtail to distant tail regions the average diameter of the flux ropes was about  $10 R_E$ , and in several instances they may be as small as 1–3  $R_E$ . The origin of these flux ropes in the magnetotail has been attributed to the currents that are generated when the ions become unmagnetized so that the Hall term in the modified Ohm's law is nonnegligible. *Slavin et al.* [2003a, 2003b] have demonstrated, using Geotail, that the flux ropes in the near-Earth region have relatively small sizes of 1–4  $R_E$ , much smaller than the plasmoids in MHD models, yet are much larger than ion skin depth sizes. In addition, *Slavin et al.* [2003a, 2003b] have asserted that these flux ropes can propagate earthward as often as tailward. The presence of earthward moving flux ropes has recently been confirmed by Cluster observations of *Zong et al.* [2004]. The development of such earthward moving flux ropes is missing from all existing global MHD models.

[10] Part of the problem/solution to understanding the magnetospheric manifestations of substorms is that the magnetospheric response is much more complicated than suggested in both the NENL and CD models. By recognizing the existence of a plethora of other processes concurrent with substorm development, one may begin to peel away the controversy and aid in a deeper understanding of the magnetospheric response to auroral substorms. To incorporate the broad range of processes one needs to fully incorporate magnetospheric-ionospheric coupling [*Kan*, 1998]. These processes include the following.

[11] 1. During current sheet thinning, the tail current sheet thins down from about 1 Earth radius to  $\sim 400$  km, which is close to the ion inertial length [*Nakamura et al.*, 2002]. For such thin current sheets, the Hall term in the generalized Ohm's law becomes nonnegligible. The corresponding Hall currents have been recently confirmed by Geotail observations [*Nagai et al.*, 2003]. The ability of Cluster to differentiate spatial and temporal structures has also brought forth definitive evidence for a highly kinked magnetotail [*Volwerk et al.*, 2003] which is subject to bifurcation [*Runov et al.*, 2003] with multiple reconnection events forming simultaneously in the magnetotail [*Eastwood et al.*, 2005].

[12] 2. Bursty bulk flows (BBFs) are observed between  $\sim 9$  and  $\sim 19 R_E$  down the tail with have speeds of 400 to 1500 km/s [*Baumjohann et al.*, 1990; *Angelopoulos et al.*, 1992] and are thought to be a result of tail reconnection located at  $\sim 20$ – $30 R_E$  [*Nagai et al.*, 1998]. These flows appear to last only a few minutes and their braking at the inner edge of the plasma sheet has been proposed as a

mechanism for generating substorm onset [Shiokawa *et al.*, 1997; Angelopoulos *et al.*, 1999].

[13] 3. Dipolarization is typically associated with changes in the  $x$  and  $z$  components of the magnetic field of the order of 10 nT at 6–10  $R_E$ , and occurs on times scales of less than 1 min [Kokubun and McPherron, 1981; Ohtani *et al.*, 1992].

[14] 4. Substorm onset is accompanied by the injections of energetic particles near the inner edge of the plasma sheet, also known as substorm injections [Arnoldy and Chan, 1969; McIlwain, 1974]. These injections are seen as a sharp increase in electron and proton fluxes over a wide range of energies and appear to propagate earthward. Satellites inside geosynchronous orbit typically observe dispersionless injections several minutes after they are observed at geosynchronous orbit with an average propagation speed of 24 km/s [Reeves *et al.*, 1996].

[15] 5. Enhanced ionospheric outflows with increased relative  $O^+$  occurred with increased activity. Korth *et al.* [2002] showed that storm time substorms can have ratios of  $O^+/H^+$  of several hundred percent, while non-storm time substorms have  $O^+/H^+$  ratios of  $\sim 15$ –65%. Even for these smaller values,  $O^+$  is a significant factor to the total energy density. Nosé *et al.* [2000, 2001] have also noted an order of magnitude increase in the relative energy density of  $O^+$  in the near-Earth region between quiet and storm time activity. Recent observations from the Cluster mission have shown that during geomagnetically disturbed times, thin current sheets are observed. Within these thin current sheets the  $O^+$  number density close to the reconnection X line in the Earth's magnetotail can become comparable to, or even higher than, the corresponding  $H^+$  number density, and the oxygen ions carry most of the particle pressure [Kistler *et al.*, 2005; Harnett *et al.*, 2008].

[16] Initial multifluid/multiscale simulations of the thinning of the plasma sheet during southward IMF were presented by Harnett *et al.* [2006]. This work demonstrated the ability to resolve ion skin depth and ion cyclotron processes within a global model and showed the presence of a thin (400 km) current sheet, which developed after the ejection of a plasmoid, with similar properties to those reported by Nakamura *et al.* [2002]. Within this current sheet, the electrons dominate the plasma pressure in its center on scale lengths of the order of the ion skin depth, the light ions on the scale length of proton gyroradius, while the  $O^+$  gyroradius appeared to be correlated with large-scale structures, including the kinking of the plasma sheet.

[17] In this paper, we utilize the multifluid/multiscale model to evaluate the dynamics of the tail in relation to substorm dynamics with an emphasis on the timing of relevant features, and to then compare the derived timing with the above observed features. This comparison serves two purposes. The first is that it allows one to examine what processes are included or neglected within the multifluid model. This model has been used successfully in a variety of space physics applications (see section 2), and it is important to quantify its predictions for substorm processes. The second is that by providing a global viewpoint that is able to include ion skin and ion cyclotron processes in the vicinity of thin current sheets, one might be able to differentiate processes related to the CD and NENL models

and thereby resolve some of the controversy between models, and provide a clearer insight into substorm development. For simplicity, this paper only considers the case of continuous southward IMF over a period of 2 h. As such, this case study provides information for internally triggered substorms. As noted above, only about 30% of the substorms appear to be internally triggered. In a later paper we will consider conditions for externally driven substorms. The case of internally triggered substorms sets up the time scale under which constant solar wind conditions can trigger a substorm. Perturbations arising from solar wind changes on shorter/longer times scales can produce modifications to the trigger and/or modify the subsequent magnetospheric activity.

[18] In section 2 we discuss the details of the model, including the multifluid and multiscale components of the model. It is shown that once a model resolves ion skin depth and ion cyclotron processes in the magnetotail, it is able to pick up the auroral currents near midnight, and as such provide an important link into understanding how substorms develop. In section 3 we show the evolution of the magnetosphere from global and regional viewpoints, including the development of plasmoids, flux ropes, auroral field aligned currents, and substorm onsets. A key result of section 3 is that X line reconnection along with the ejection of the plasmoid is a transient that is several minutes earlier relative to substorm onset, consistent with Baker *et al.* [2002]. At best, the X line formation and ejection of the plasmoid are correlated with pseudobreakup and not substorm onset.

[19] In the postplasmoid current sheet (section 4), plasma convection drives the development of a Y line (as opposed to an X line) current sheet. Within this thin straight current sheet, small-scale flux ropes are generated on the scales sizes noted by Slavin *et al.* [1995] and Lepping *et al.* [1995, 1996]. Flux ropes develop that propagate both tailward and well as earthward with equal numbers consistent with Slavin *et al.* [2003a, 2003b] and Zong *et al.* [2004]. The presence of equal numbers of differently directed flux ropes arises from the fact that there is partial reflection of energy between the inner edge of the plasma sheet and the trailing edge of the ejected plasmoid/X line. The buildup of energy from continued current sheet acceleration and the above partial reflection of energy leads to the intensification and size of the flux ropes being generated within the Y line (section 5). Dissipation of this energy associated with large earthward moving flux ropes at the inner edge of the plasma sheet generates substorm onset. Thus, while reconnection is occurring during substorm development, the actual “trigger” for substorm onset occurs at the inner edge of the plasma sheet.

[20] In section 6 we detail the local characteristics that would be observed by a spacecraft. We show that the model is able to generate pseudobreakup signatures during growth phase similar to that of Takada *et al.* [2008], plus rapid dipolarization on the order of a minute at onset, consistent with Ohtani *et al.* [1992], along with multiple current sheet crossings generated by the kinking of the thin plasma sheet in a manner consistent with the observations of Runov *et al.* [2003]. We show that ionospheric  $O^+$  is late in arriving in the tail for pseudobreakup but is a significant factor at onset.

Conversely, fast flows first appear near pseudobreakup, and prior to and through substorm onset. The bursty nature of the fast flows are actually due to the inherent 3-D nature of the plasma sheet with fast flows being present essentially continuously, but moving around in space. As such, bursty bulk flows are part of the entire substorm dynamics but are not the actual trigger for onset.

[21] The above features appear to account for multiple observed features of substorms. The synthesis of results indicates that a model that combines features of the NENL and CD models resolves the controversy between models and potentially yields a more accurate description of processes leading to the development of substorms. Energy flow between the X line and inner edge of the plasma sheet is an integral part of the synthesis model. The appearance of different processes relative to substorm onset is described in section 7.

## 2. Ion Cyclotron/Ion Skin Depth Effects in the Multifluid/Multiscale Model

[22] The first attempts to incorporate Hall effects into a 3-D global model used a perturbation expansion [Winglee, 1994] valid for  $|V \times B| \gg |J \times B|/en$ , and provided a first glimpse of how the magnetic topology predicted by MHD would be modified by a small, but nonzero, Hall correction. Because of the ordering of terms with  $|V \times B| \gg |J \times B|/en$ , this solution is only valid for  $V \neq 0$ . The model was subsequently improved to fully incorporate the Hall and  $\nabla P$  terms without any perturbation approximation, and demonstrated that even at a course resolution of 0.25  $R_E$ , these corrections could produce a core magnetic field comparable to that observed in tail flux ropes [Winglee *et al.*, 1998]. With the evolution of the multifluid model, different sources of ions could be tracked and this work led to the first three dimensional identification of the geopause, as well as a description of the relative roles of ionospheric and solar wind plasma in populating the magnetosphere [Winglee, 1998, 2000], the importance of ionospheric mass outflows in mass loading of the magnetosphere, the generation of the Harang discontinuity, and the cross polar cap potential [Winglee *et al.*, 2002, 2005; Winglee, 2004]. Excellent agreement with observations has been obtained for weakly magnetized systems such as Mars and Ganymede [Harnett and Winglee, 2003, 2007; Paty and Winglee, 2004, 2006]. Asymmetric pickup of heavy ions at Pluto, as seen in hybrid codes but not MHD, has also been demonstrated within the multifluid approach [Harnett *et al.*, 2005]. Comparative studies within the terrestrial magnetosphere have also been successful in quantifying the different populations with the magnetosphere [Winglee *et al.*, 1998; Li *et al.*, 2000] and the development of flux ropes at the magnetopause [Winglee *et al.*, 2008a].

[23] The most recent version of the code fully incorporates ion skin depth effects in Ohm's law and ion cyclotron terms in the momentum equation that leads to current sheet acceleration [Winglee *et al.*, 2005]. This model has been used to account for many of the features of flux transfer events at the magnetopause [Winglee *et al.*, 2008a], and the local time variations in ionospheric outflows [Winglee *et al.*, 2008b]. The specifics of the code are as follows. The dynamics of each plasma component are described by mass,

momentum and pressure equations given by [Krall and Trivelpiece, 1972]

$$\frac{\partial \rho_\alpha}{\partial t} + \nabla \cdot (\rho_\alpha \mathbf{V}_\alpha) = 0 \quad (1)$$

$$\rho_\alpha \frac{d\mathbf{V}_\alpha}{dt} = q_\alpha n_\alpha (\mathbf{E} + \mathbf{V}_\alpha \times \mathbf{B}(\mathbf{r})) - \nabla P_\alpha - \left( \frac{GM_E}{R_e^2} \right) \rho_\alpha \mathbf{r} \quad (2)$$

$$\frac{\partial P_\alpha}{\partial t} = -\gamma \nabla \cdot (P_\alpha \mathbf{V}_\alpha) + (\gamma - 1) \mathbf{V}_\alpha \cdot \nabla P_\alpha, \quad (3)$$

where the subscript  $\alpha$  denotes the ion and electron components that constitute the plasma. In hybrid codes and in the multifluid code, one makes the assumption that the electrons are a fluid and that they have sufficiently high mobility along the field lines such that they are approximately in steady state (i.e.,  $d/dt = 0$ ), or in drift motion. This assumption removes high-frequency plasma waves and electron waves but enables the momentum equation for the electrons to be reduced to

$$\mathbf{E} + \mathbf{V}_e \times \mathbf{B} + \frac{\nabla P_e}{en_e} = 0. \quad (4)$$

The electron dynamics are completed by assuming quasi-neutrality, and applying the definitions for current and electron pressure. For a single component plasma one obtains

$$N_e = N_i, \quad \mathbf{V}_e = \mathbf{V}_i - \frac{\mathbf{J}}{en_e}, \quad \mathbf{J} = \frac{1}{\mu_0} \nabla \times \mathbf{B} \quad (5)$$

$$\frac{\partial P_e}{\partial t} = -\gamma \nabla \cdot (P_e \mathbf{V}_e) + (\gamma - 1) \mathbf{V}_e \cdot \nabla P_e. \quad (6)$$

The magnetic field is obtained by using the electric field (4) in the induction equation:

$$\frac{\partial \mathbf{B}}{\partial t} + \nabla \times \mathbf{E} = 0. \quad (7)$$

In the multifluid treatment, we assume three different ion components: (1) solar wind protons, (2) ionospheric protons, and (3) ionospheric oxygen ions. With these multiple components present, charge and current density are completed by

$$n_e = \sum_i (q_i/e) n_i, \quad \mathbf{V}_e = \sum_i \frac{q_i n_i}{en_e} \mathbf{V}_i - \frac{\mathbf{J}}{en_e}, \quad \mathbf{J} = \frac{1}{\mu_0} \nabla \times \mathbf{B}. \quad (8)$$

Substitution of (8) into (4) yields a modified Ohm's law:

$$\mathbf{E} = - \sum_i \frac{q_i n_i}{en_e} \mathbf{V}_i \times \mathbf{B} + \frac{\mathbf{J} \times \mathbf{B}}{en_e} - \frac{1}{en_e} \nabla P_e + \eta(\mathbf{x}) \mathbf{J}. \quad (9)$$

The first term in (9) is the ideal Ohm's law. The last term,  $\eta(\mathbf{x}) \mathbf{J}$ , is added to allow for finite conductivity in the

ionosphere only. Collisions beyond this region are assumed to be negligible. No anomalous resistivity is included in the code. Note that the Hall and  $\nabla P_e$  terms scale with the ratio of the ion skin depth to the current sheet thickness. If one substitutes the electric field (9) into the ion momentum equation one obtains

$$\begin{aligned} \rho_\alpha \frac{dV_\alpha}{dt} = & q_\alpha n_\alpha \left( \mathbf{V}_\alpha \times \mathbf{B}(\mathbf{r}) - \sum_i \frac{q_i n_i}{en_e} \mathbf{V}_i \times \mathbf{B} \right) \\ & + q_\alpha n_\alpha \left( \frac{\mathbf{J} \times \mathbf{B}}{en_e} - \frac{1}{en_e} \nabla P_e \right) - \nabla P_\alpha - \left( \frac{GM_E}{R^2} \right) \rho_\alpha \vec{r}. \end{aligned} \quad (10)$$

The first term in (10) is dropped in MHD. If this is done and a single species is assumed, (10) reduces to the ideal MHD momentum equation. In reality, the presence of different ion species or energy populations means that the first term ( $\mathbf{V}_\alpha \times \mathbf{B} - \sum_i (q_i n_i / en_e) \mathbf{V}_i \times \mathbf{B}$ ) is invariably nonzero in weakly magnetized regions but almost zero in strongly magnetized regions. In the weakly magnetized regions the nonzero difference (i.e., the first term on the right-hand side of (10)) drives ion cyclotron effects, which becomes important as the gyroradius becomes comparable to the scale length of the current sheet, and in fact for heavy ions like  $O^+$  this term can dominate acceleration. As demonstrated below, a key signature of this effect is that in the presence of thin current sheets near substorm onset  $O^+$  ions can have a bulk velocity primarily in the dawn/dusk direction because of electric field acceleration while  $H^+$  ions interacting with the same electric field under  $\mathbf{E} \times \mathbf{B}$  drift motion with flows primarily earthward or anti-earthward.

[24] While the above equations incorporate ion skin depth and ion gyroradius effects, resolving all scale lengths over the entire global system is problematic at best. A tractable solution is obtained by noting that in the strongly magnetized regions around the earth, the particle trajectories derived from particle tracking are consistent with simple convective drift motion and therefore we do not attempt to resolve skin depth and gyroradius effects in these regions [Winglee, 2003]. However, in the weakly magnetized regions around the tail and magnetopause current sheets the particle dynamics can differ significantly from MHD treatments where the proton skin depth can be a few hundred kilometers and its gyroradius several hundred kilometers. For  $O^+$ , the skin depth can be several hundred kilometers and its gyroradius a few thousand km. At these scale lengths the presence of thin current sheets with a width of 800 km violates the assumptions that are made in formulating the MHD equations. The above multifluid equations lead to consistent flows between the particle and fluid methodologies when in the presence of thin current sheets that form during southward IMF. Under these conditions, ion acceleration as opposed to drift motion occurs whenever the external solar wind conditions lead a current sheet where its thickness is less than about the ion gyroradius [Winglee, 2004].

[25] Running high-resolution simulations for the global magnetosphere is computationally very expensive. In order to obtain a tractable solution, we first run the code with a stack set of grid systems with a base resolution similar to that used in past simulations to set up a 2-h equilibrium for

the magnetosphere under quiescent conditions and within which the tail current is relatively thick. In the following, a zero IMF equilibrium is established for nominal solar wind conditions of a density of  $6 \text{ cm}^{-3}$  and a speed of 450 km/s. The base grid system has a grid spacing of  $0.3 R_E$  in the inner magnetosphere. In the midtail to distant tail, the grid spacing is increased from 0.3 to  $2.4 R_E$  across the nested grids with the largest grid covering in the distant tail to  $x \sim -200 R_E$  (GSM), and at the flanks at  $\pm 60 R_E$  with the solar wind boundary is at  $x = 35 R_E$ . The inner radius of the simulations is set to  $2.7 R_E$ . The region within the inner boundary is given a finite resistance equivalent to a Reynolds number of 10. At the actual inner boundary (representing the ionosphere), the Reynolds number is increased to 20 and at one grid point above it is set at 40. At all other points the resistivity is zero. These values yield an overall height integrated resistivity of about  $10^5 \text{ Ohm m}^2$ , which is of the order of the height integrate resistivity of the ionosphere at about 100 km [Kelley, 1989]. The corresponding resistance over the auroral zone yields approximately 0.15 mOhm.

[26] After the above equilibrium is established the IMF is turned southward to  $-5 \text{ nT}$  at  $t = 0200 \text{ h}$ , with other solar wind conditions being kept constant. At the same time refinement gridding is applied to the base grid system of the tail region with a series of overlaying grids giving finer resolution of the tail. Since there is a finite propagation time of the solar wind to the magnetopause and the penetration of fields into the plasma sheet there is more than sufficient time for the current sheet to come into equilibrium with the refinement gridding before the influence of the southward IMF is felt. In the present case the resolution is set at 900 km for  $-3 < x/R_E < -33$  and  $y$  and  $z$  between  $\pm 10 R_E$ , and 450 km resolution is used between  $-9 < x/R_E < -20$  and  $y$  and  $z$  between  $\pm 5 R_E$ . This resolution is a factor of 4 coarser than used by Harnett *et al.* [2006] but shows the same basic features associated with a very thin current sheet. The coarser resolution allows longer-duration simulations and an examination of a great part of parameter space.

[27] The temperature profile around the inner boundary is also similar to previously published versions of the multifluid model. At the equator, a high temperature of 20 eV is assumed. The plasma temperature then decreases with increasing latitude, reaching a minimum of 0.1 eV at the poles. The high temperature at the equator represents the hotter plasma trapped on closed field lines, while the low temperature over the polar cap is typical for the polar cap ionosphere. The density at the equator is assumed to be  $800 \text{ cm}^{-3}$ , which is of order of the plasmaspheric density at the radial distance of the inner boundary. Because of the low temperature assumed over the poles, the mobility of the plasma is very small so that we assumed only a slight decrease in density with latitude, with a minimum density at the poles of  $400 \text{ cm}^{-3}$ . This density is typical of the topside ionosphere over the polar cap. One difference with previous applications of the model is that we included a variable  $O^+$  density in the vicinity of the auroral oval with a 5% concentration at auroral latitudes which then decreases to zero at both the poles and at the equator.

[28] These equations and boundary conditions are solved using a second-order Runge-Kutta method with Lapidus correction on the above structured grids and using standard second-order difference schemes for the spatial derivatives.

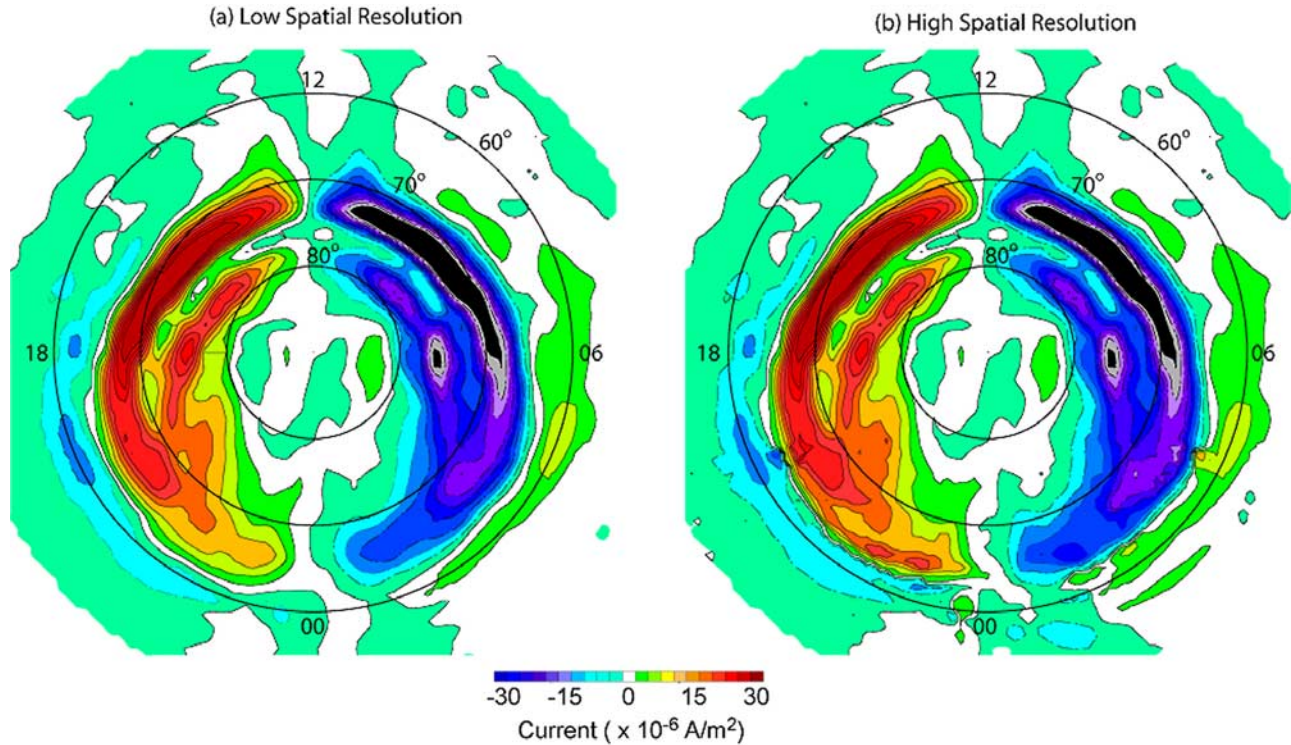


**Figure 1.** Comparison of the auroral currents using (a) only the base grid system with 1800 km resolution and (b) using the refinement grids with resolution of 450 km at  $t = 0246$ . With the increased spatial resolution more intense auroral currents near midnight are obtained.

The introduction of Lapidus smoothing introduces only third-order corrections to the above equations on an inherently second-order scheme. As such the only area where the correction has significant effects is in the vicinity of the shock region where grid point oscillations can develop. The correction leads to the removal of the oscillations and the sharpening of the shock properties consistent with the Rankine-Hugoniot relations.

[29] The time step is set as the minimum over the grid of the  $0.1 \Delta x/V_{\max}$ , and  $0.2/\Omega_{i,\max}$ , where  $V_{\max}$  is the maximum of the bulk speed, sound speed and Alfvén speeds,  $\Omega_{i,\max}$  is the maximum ion cyclotron frequency. The cutoff for the whistler wave that is incorporated within the grid system is dependent on the spatial resolution of the grid. Thus for the coarse grid system the whistler cut off is comparable to the ion cyclotron frequency and the ion plasma frequency is not resolved. In the refined grid system, the ion skin depth is comparable to the grid spacing and the ion plasma frequency has to be resolved. In these regions the Alfvén speed in the lobes is tens of thousands of km/s and sets the time step. Under these conditions, since  $\Delta x \sim c/\omega_{pi}$  and  $V_A = c \Omega_i/\omega_{pi}$  so that the ion plasma frequency is resolved in the reconnection region.

[30] The largest grid system is first stepped in time, and the derived quantities are used as outer boundary conditions for the next grid system which lies within it. The derived quantities from the smaller but higher-resolution grid system are used as inner boundary conditions for the larger box that it is nested within. This process is repeated downward for the series of nested set of grids.

[31] As previously noted by *Winglee* [2004], the addition of ion skin and ion cyclotron effects leads to the enhancement of the auroral current system near midnight. With the increased grid resolution provided by the refinement gridding we are able to demonstrate further enhancement of these currents; that is, the nightside auroral currents are associated with small-scale processes in the tail and not with the large-scale MHD currents. Figure 1a shows the derived field-aligned current density mapped down to the Earth's surface when only the low-spatial resolution grid system is used to derive the currents. The mapping of the current assumes that the total current is conserved and that the area of the current maps along dipole-like field lines so that the area goes as  $R^3$  and the values shown are what would be observed at 100 km altitude.

[32] The overall structure of Region 1 and 2 currents is obtained, but with very little current near midnight. There is a double auroral current in the Region 1 currents and this splitting of the current is directly due to the gradients in the heavy ion density and pressure which varies across the inner boundary of the auroral zone. This fine structure within the auroral oval can be induced by heavy ion variations in the ionosphere. With the inclusion of the refinement grid points in the tail, a substantial augmentation of the currents is seen near midnight with their current density being comparable to the dayside Region 1 current intensities.

[33] This augmentation arises because the high spatial resolution (Figure 1b), particularly near the inner edge of the plasma sheet, allows a more accurate treatment of small-scale but intense currents associated with ion skin depth and ion cyclotron effects. These effects are known to generate

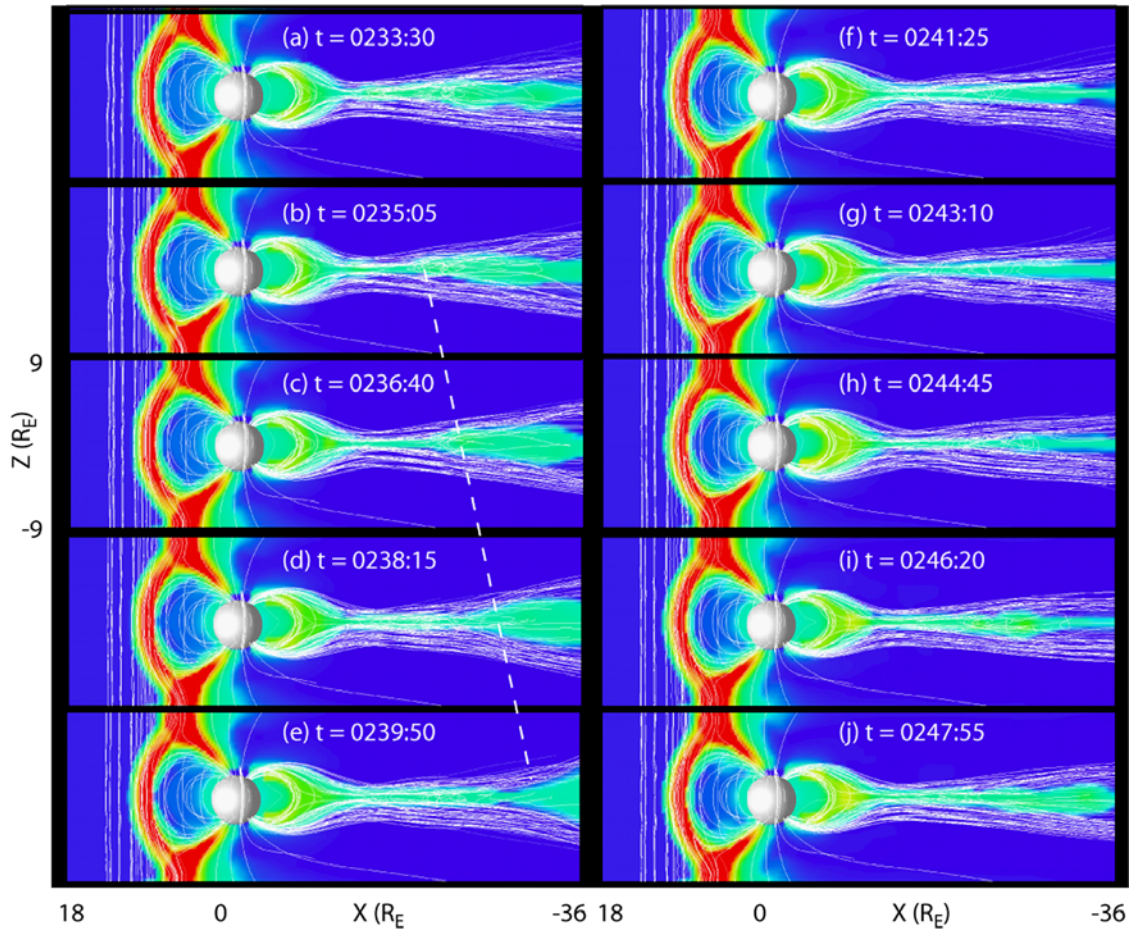


**Figure 2.** Large-scale view of the evolution of the magnetic field and total plasma pressure through the noon-midnight meridian. An X line forms at  $t = 0235$  in association with the ejection of a plasmoid which is about  $10 R_E$  long. The movement of the rear of the plasmoid is indicated by the dashed white line. In the wake of the plasmoid a Y line forms, where the field lines are essentially parallel to the equator from 10 to  $25 R_E$  and there is transient reconnection that leads to the generation of smaller flux ropes with lengths of  $2-3 R_E$ .

an in-plane magnetic field parallel/antiparallel to the tail current sheet. The corresponding current has a field-aligned component and these currents flow into the ionosphere. It is possible that the currents derived in the present model still underestimate the actual peak currents that can develop in the region. The main point is that we are starting to resolve the midnight currents, enabling us to correlate auroral processes with magnetospheric processes during the development of a substorm. This correlation is the focus of section 3.

[34] The magnitudes of the currents are also interesting to examine. Taking the derived currents and remapping then to FAST altitudes of 4000 km would yield peak currents in the nightside of  $1-3 \mu A/m^2$  for the lower resolution (Figure 1a) and  $4-8 \mu A/m^2$  for the higher-resolution gridding (Figure 1b). The latter lies with the  $5-10 \mu A/m^2$  range seen in FAST observations [e.g., *Elphic et al.*, 1998; *Le et al.*, 2002]. The currents reported here lie below the  $200 \mu A/m^2$  (mapped to the ground) observed by Viking [*Potemra et al.*, 1988]. A recent statistical model shows peak currents of  $<1 \mu A/m^2$  [*Papitashvili et al.*, 2002]. Presumably these currents are much smaller than currents associated with a single event

because the statistical approach leads to an averaging over phenomena that can change the position (in both local time and latitude) for the currents which can also have substantial time variations. The time and spatial variations which are the focus of the present study are averaged out in the statistical studies of *Papitashvili et al.* [2002].

### 3. X Line Formation and Pseudobreakup

[35] A large-scale view of the tail dynamics is shown in Figure 2. The high-resolution gridding is incorporated but within this global view point only the large-scale features can be seen. These smaller-scale features are discussed in sections 4 and 5. The important point here is that the large-scale view is typical of many global models. Under the influence of southward IMF, pinching of the tail occurs between 15 and  $20 R_E$  (Figure 2a) and this leads to the development of an X line and the ejection of a plasmoid (Figures 2b and 2c). This plasmoid is greater than  $10 R_E$  in length. The timing of the ejection and the size of the plasmoid is dependent on the prevailing solar wind con-

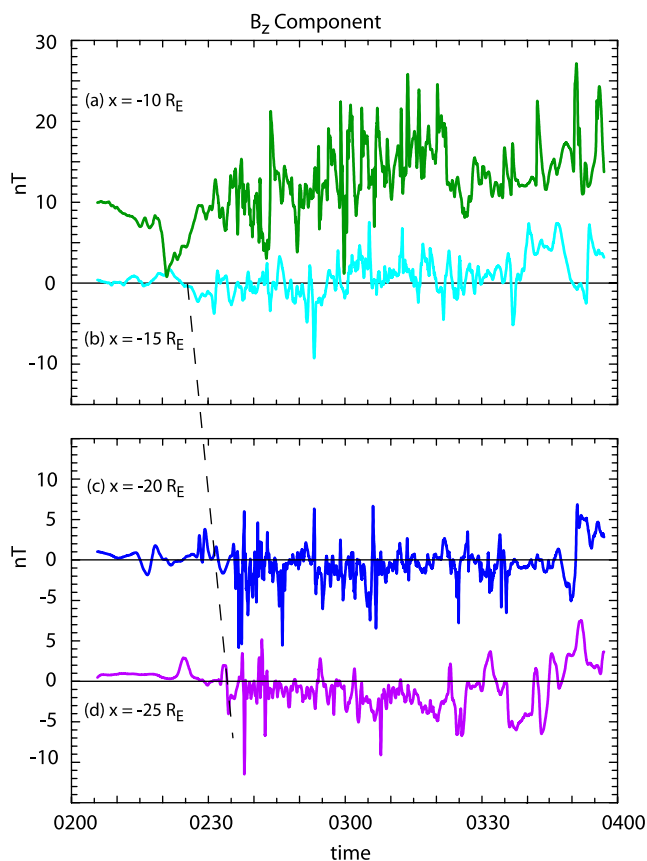


**Figure 3.** Evolution of  $B_z$  at four positions down the tail:  $(-10, 0., 0.5) R_E$  (curve a),  $(-15, 0., -0.5) R_E$  (curve b),  $(-20, 0., 0.) R_E$  (curve c), and  $(-25, 0., 0.) R_E$  (curve d). The dashed lines show the propagation of the reconnection down the tail.

ditions. If the prevailing IMF were northward as opposed to the zero IMF prior to the southward turning, then the formation of the X line would be delayed and a larger plasmoid would be ejected down the tail.

[36] The ejection of the plasmoid from the near-Earth plasma sheet in association with the tailward movement of the X line occurs after another 10 min. In the wake of the plasmoid, a thin current sheet is formed (Figures 2f–2i) where the field lines are essentially parallel to the equatorial plane. The Y line as opposed to X line forms because the system is convectively dominated with fast flows in the  $x$  direction, so that the convection rate dominates the dissipative processes that would favor the development of an X line.

[37] The exact timing of reconnection in the tail can be determined quantitatively from Figure 3 which shows the time histories of  $B_z$  at four different positions down the tail. In order to maximize coverage, the samples are taken at  $5 R_E$  intervals starting near the inner edge of the plasma sheet at  $x = -10 R_E$  down the tail. The first 2 positions are displaced  $\pm 0.5 R_E$  off the equator so that there is a nonzero  $B_x$  component in the equilibrium fields, so that tail stretching and dipolarization can be easily seen. The two more distant sample positions are taken exactly on the magnetic equator so that warping of the tail as seen by crossings between the northern and southern hemispheres could be seen more easily seen.

[38] Dayside reconnection leads to enhanced convection into the tail which appears as a reduction in  $B_z$  at  $x = -10 R_E$  starting at 0220 UT. However,  $B_z$  does not turn negative at this point. Instead, the first negative  $B_z$  is seen at  $x = -15 R_E$  at 0225 UT and this reconnection signature is seen to move outward at  $1 R_E/\text{min}$  with negative  $B_z$  developing at  $x = -25 R_E$  at 0335 UT. Thus the ejection of the X line at  $100 \text{ km/s}$  is slower than the ejection of the plasmoid itself which is traveling at about  $400 \text{ km/s}$ . The very short spiky negative  $B_z$  features (e.g., at  $x = -20 R_E$ ) are associated with flux ropes which will be described in more detail in sections 4 and 5.

[39] The reconfiguration of the tail in Figure 2 is exactly consistent with the development of the NENL as proposed by Hones [1984]. The question that we have not addressed is the timing of the above processes relative to substorm onset. There are two ways in which we can relate the tail processes with substorm onset. The first is to examine the evolution of the auroral currents as shown in Figure 4. Associated with the increased convection into the tail, there is an enhancement in the nightside currents (Figures 4a–4d), but the intensity is not sufficient for a substorm. The enhancement of the currents in general increases continuously from the dayside to the nightside though, for example, there is a jump in the current intensity that appears at 22 MLT before it intensifies at 21 MLT (Figure 4c). The nightside currents are primarily confined near the equatorward edge of the auroral oval until  $t \sim 0240$  when there is an intensification of the currents near midnight and an expansion of these currents into the auroral oval (Figure 4e). This intensification declines by 0246 (Figure 4g).

[40] The timing of the nightside currents relative to the reconnection in Figures 2 and 3 is very informative. The brightening and poleward expansion of the auroral currents occurs approximately 6 min later in association with the ejection of the plasmoid/reconnection signatures seen at the spacecraft at  $\sim 20 R_E$  down the tail. This delay time is consistent with that noted by Baker *et al.* [2002]. However, the duration of the current enhancement is only about 10 min, which is the time scale of a pseudobreakup and is too short for typical substorm intensifications with average durations of 30 min. The time of this auroral intensification corresponds to a short-lived increase in  $B_z$  at the spacecraft at  $10 R_E$  which is supportive of the identification of this period as a pseudobreakup and not substorm onset. As demonstrated below there is insufficient energy available at this early stage to drive a substorm.

[41] As a second method to determine the timing of substorm onset we investigated the time histories of  $B_x$  down the tail as shown in Figure 5. For the first two positions where there is displacement from the equator, the stretching of the tail field lines is clearly seen as an increase in the magnitude of  $B_x$ . The field lines reach their most stretched configuration at  $t = 0228$  at  $x = -10 R_E$  and at  $t = 0232$  at  $x = -15 R_E$ . Shortly after this time, X line formation occurs as noted in Figure 2. Near the inner edge of the plasma sheet a brief dipolarization occurs between 0240 and 0243 (Figure 5, green curve). This time period corresponds to the intensification and poleward expansion of the auroral currents near midnight in Figure 4. The dipolarization is short lived with the  $B_x$  field returning to a stretched configuration until  $t = 0258$  (Figure 5, green curve). At this time, rapid dipolariza-

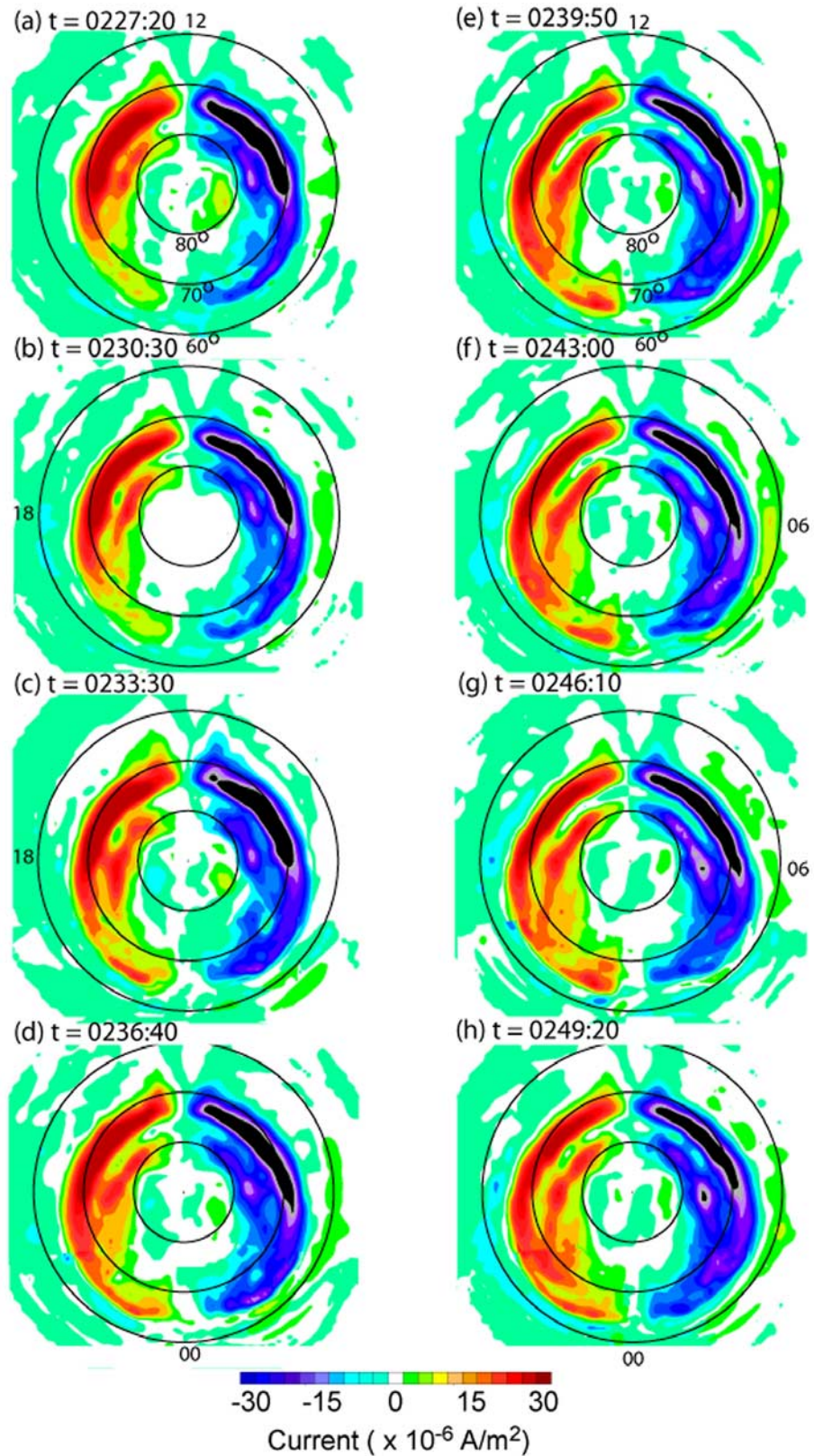


**Figure 4.** Evolution of the auroral currents. The nightside currents first strengthen along the equatorward edge. At  $t = 0240$  the currents near midnight intensify and expand poleward. This enhanced activity lasts for about 10 min.

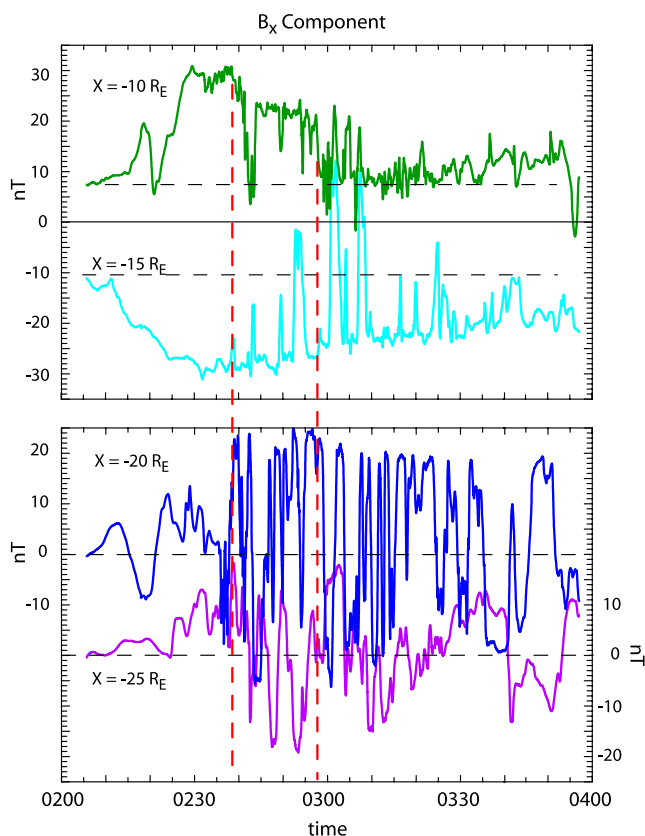


**Figure 5.** Evolution of  $B_x$  at the same four positions in Figure 3. The black horizontal dashed lines show the equilibrium values of  $B_x$  prior to the southward turning of the IMF. The red vertical lines indicate the start of a short-lived dipolarization (pseudobreakup) at the spacecraft at  $10 R_E$ . True dipolarization (substorm onset) does not occur until 0258 where  $B_x$  returns to its initial value. At larger distances, full dipolarization is not seen. Instead there are multiple and rapid crossings of the plasma sheet which is associated with the kinking of the thin tail current sheet.

tion occurs within 1 min with the magnetic field strength then dropping to the essentially the field strength prior to the southward IMF turning. It stays on average at this field strength for approximately 30 min. At the same time there is also a rapid and sustained increase in  $B_z$  (Figure 3, curve a) at  $x = -10 R_E$ , also indicative of dipolarization. These changes in the magnetic field profile and the time scale for dipolarization are consistent with *Kokubun and McPherron* [1981] and *Ohtani et al.* [1992].

[42] The above timing is a crucial result. While the results have the tail evolving essentially in the same manner as outlined in the NENL, X line reconnection and the ejection of the plasmoid occur well before onset. They are more closely associated with pseudobreakup. In section 4 we will examine the processes that are directly responsible for the auroral enhancements and substorm onset.

#### 4. Flux Ropes and Pseudobreakup

[43] The above results indicate that while X line reconnection and plasmoid ejection are fundamental tail processes,

they are not directly related to substorm onset. At best they appear as precursors to substorm onset. If this is the case, then the question becomes what is the actual trigger for the auroral substorm? This question is taken up in this section. A key aspect of the solution to this problem is that the large-scale view of Figure 2 misses the small-scale dynamics of suggested by the magnetic signatures in Figures 3 and 5, and it is these small-scale processes that are directly tied to substorm onset. These effects are illustrated in Figure 6 which shows a high-resolution view of a  $13 R_E$  span of the plasma sheet starting from its inner edge. This section is the thinnest part of the plasma sheet. It is under the influence of enhanced tailward flows in the lobe and enhanced earthward flows originating from the X line, which is further down the tail. Because of the inhomogeneous nature of these flows, localized reconnection can occur along the Y line through localized pinching of the plasma sheet. Because of the very small width of the current sheet, the influence of ion skin depth and ion cyclotron processes dominate the ion acceleration which is a key

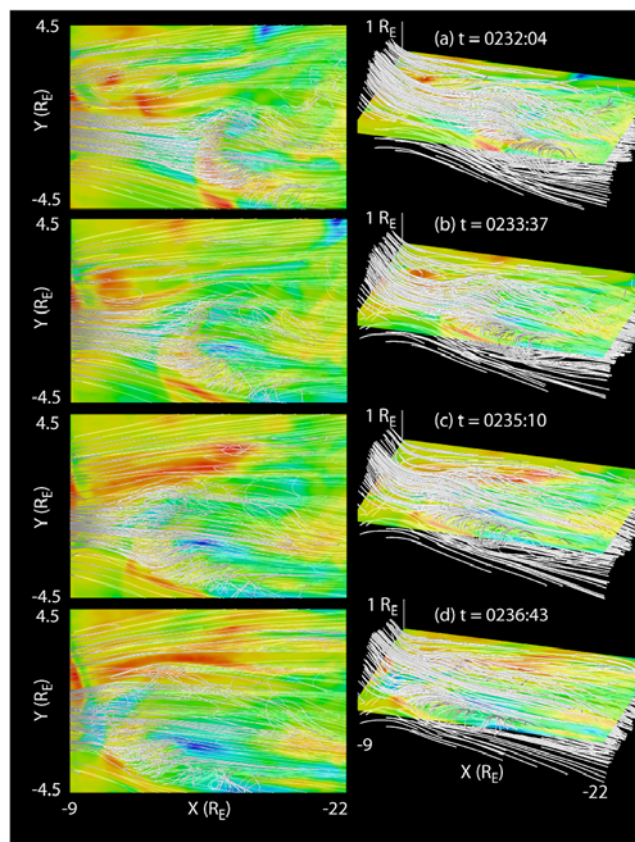


**Figure 6.** Field line mapping and the equatorial plasma pressure as seen (left) from the top and (right) from the duskside showing the development of a small-scale ( $6 R_E$  wide and  $0.5 R_E$  in height) earthward moving flux rope that impacts the inner edge of the plasma sheet. This impact leaves the field lines to be directed more vertically, i.e., more dipole-like. The pressure contours have a floating range so that local maxima relative to the position of the flux rope can be seen. These maxima occur with the flux rope but also toward the dawnside.

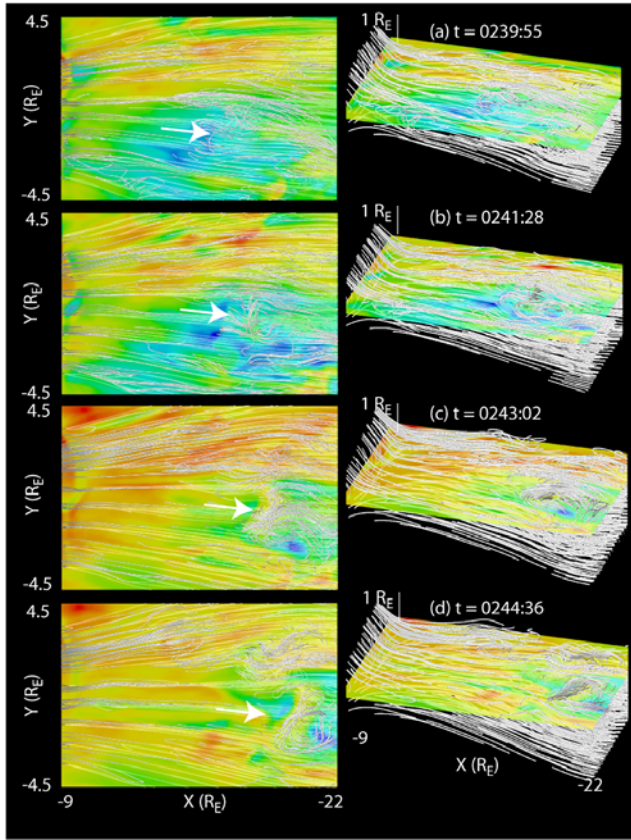


**Figure 7.** Continuation of Figure 6 showing the development of a tailward moving flux rope, initially forming at  $x \sim -15 R_E$ .

component to the generation of the flux ropes, including the presence of a strong core magnetic field, as seen in Figure 6a.

[44] It is important to note that while the overall shape of the flux ropes in Figure 6 may resemble a plasmoid, there are important differences. First, the scale size is very much smaller. They extend in  $z$  less than  $\sim 0.5 R_E$ ,  $\sim 1-2 R_E$  in  $x$  and  $\sim 5 R_E$  in  $y$ . These sizes are consistent with those reported by *Slavin et al.* [2003a, 2003b]. The other critical feature is that because they develop earthward of the X line, they can propagate either earthward or tailward, whereas the plasmoid only propagates tailward. Figure 6 shows the development of the first earthward moving flux rope that is easily identifiable within the simulations. This earthward moving flux rope is traveling at about  $2 R_E/\text{min}$  or about  $200 \text{ km/s}$  and is able to propagate all the way into the inner edge of the plasma sheet (Figure 6d).

[45] Shortly ( $\sim 3 \text{ min}$ ) after the arrival of this earthward moving flux rope at the inner edge of the plasma sheet, a tailward propagating flux rope is seen to develop near  $x = -15 R_E$ , as seen in Figure 7. This flux rope intensifies as it moves tailward as seen in the different plots of Figure 7. As noted in section 1 *Slavin et al.* [2003a, 2003b] and *Zong et al.* [2004] have reported the observation of earthward and tailward moving flux ropes with approximately even occurrence rates. In order to show that the flux ropes within the simulations have similar properties to the observed flux ropes Figure 8 shows the time histories of the magnetic field

and proton flow velocity at high time resolution at  $x = -15 R_E$  and  $-10 R_E$ .

[46] The earth moving flux ropes are seen as having first a negative  $B_z$  followed by a positive  $B_z$  signature (i.e.,  $\mp B_z$ ) as indicated by the blue dashed circles. At  $x = -15 R_E$  the flux ropes have a swing in  $B_z$  of about  $\mp 5 \text{ nT}$ . They also have a core ( $B_y$ ) magnetic field that is comparable to peak values of  $B_z$ . The duration of the flux ropes as observed by a spacecraft is about 2 min. These features are consistent with those reported by *Slavin et al.* [2003a, 2003b].

[47] The strength of the plasma flows are modified by the presence of these flux ropes. At  $x = -15 R_E$ , the first earthward moving flux rope produces a weak increase in  $V_x$  and the second earthward moving flux ropes is almost able to produce a reversal in  $V_x$ . As shown in section 5, later earthward moving flux ropes generate a strong flow reversal. Such a reversal is seen closer in at  $x = -15 R_E$ , producing bursty bulk flow features at peak speeds of about  $400 \text{ km/s}$ . The appearance of these flows relative to the magnetic structure of the flux ropes is also consistent with *Slavin et al.* [2003a, 2003b]. Note that the presence of high speeds and stronger magnetic perturbations at  $x = -10 R_E$  is indicative that these earthward moving flux ropes are subject to compression and acceleration as they move inward.

[48] The simulations do not show the presence of tailward moving flux ropes at  $x = -10 R_E$ . This is because the source region for the flux ropes is beyond this position. The tailward moving flux rope seen at  $x = -15 R_E$  has the characteristic  $\pm$  variation in  $B_z$ , and are associated with fast tailward flows. The duration of these flux ropes are also a couple of minutes. These flux ropes have variations in the field strength of  $\pm 5 \text{ nT}$  and their duration and association with fast tailward flows are all consistent with *Slavin et al.* [2003a, 2003b]. Thus, the conclusion is that the model is able to generate both earthward and tailward moving flux ropes that have been observed by *Slavin et al.* [2003a, 2003b].

[49] There are two other important features that can be seen in Figure 8. First the passage of the flux ropes causes the spacecraft to see a decrease in  $B_x$ , causing the spacecraft to appear to move closer to the center of the current sheet. As seen in the full history of  $B_x$  in Figure 5, these kinks grow in strength reaching their maximum amplitude a few minutes after substorm onset. The magnitude of these perturbations in  $B_x$  is comparable to that reported by *Runov et al.* [2003]. The periodicity of the kinks seen in the simulations is about 6 min which is about twice the period of that observed by *Runov et al.* [2003]. However, as demonstrated in section 6 the periodicity is dependent on position with higher frequencies being present further down the tail.

[50] The second important feature is that the arrival of the earthward moving flux rope at the inner edge of the plasma sheet coincides with the beginning of pseudobreakup. This pseudobreakup at  $x = -10 R_E$  takes approximately 2 min in  $B_x$ . The response in  $B_z$  is delayed by about a min relative to the  $B_x$  signature but reaches dipole-like field strengths within a 1 min. This rapid dipolarization is consistent with *Ohtani et al.* [1992].

[51] Taking the simulation density of  $0.3 \text{ cm}^{-3}$ , and a speed of  $300 \text{ km/s}$ , plasma energy flux associated with this

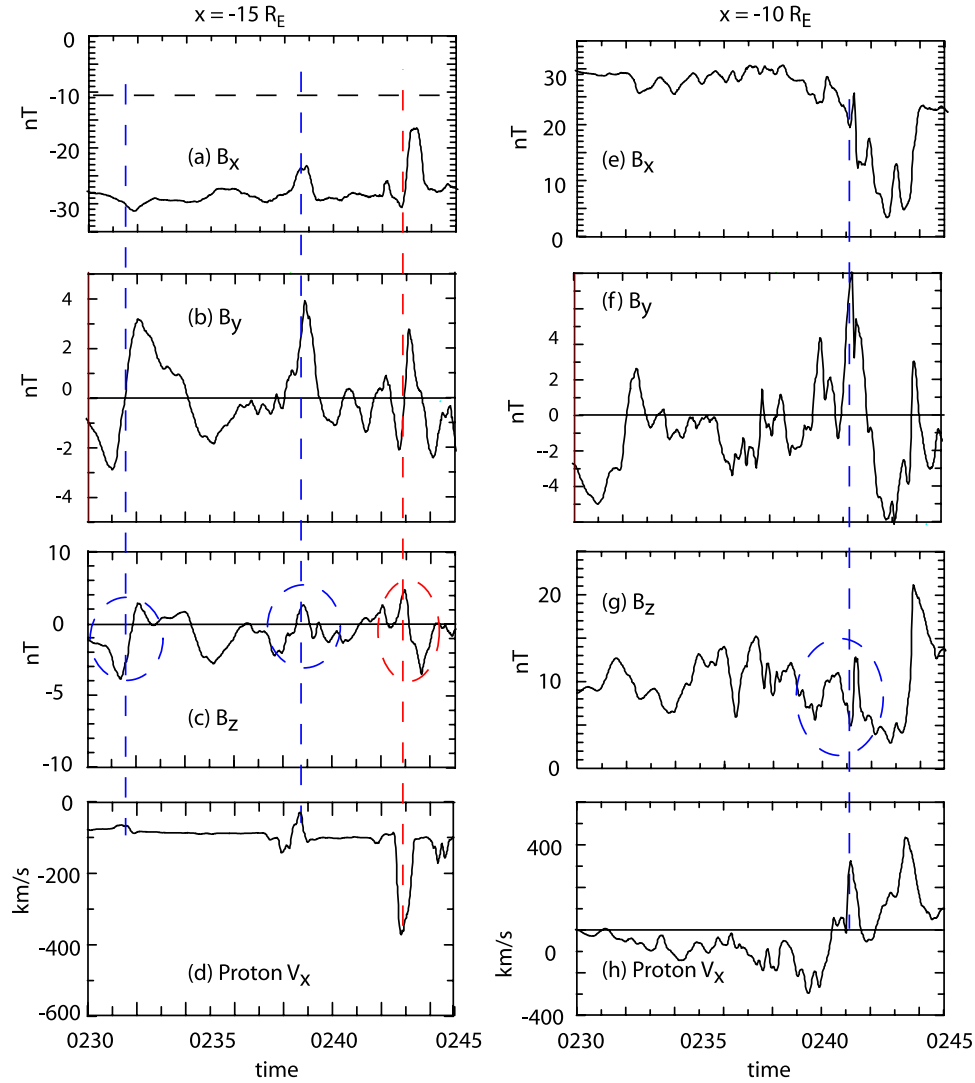


**Figure 8.** Time histories of  $B_x$ ,  $B_y$ ,  $B_z$ , and the proton  $V_x$  at (left)  $x = -15 R_E$  and (right)  $x = -10 R_E$ . The earthward moving flux ropes are indicated by the blue dashed circles, and tailward moving flux ropes are indicated by the red dashed circles.

flux rope is about  $7 \times 10^{-6} \text{ J/m}^2/\text{s}$  assuming protons only. For a magnetic perturbation of 10 nT near the inner edge of the plasma sheet, the incident magnetic flux is  $15 \times 10^{-6} \text{ J/m}^2/\text{s}$ . Integrating over the face of the flux rope the total power delivered to the edge of the inner plasma sheet is 10 GW. This energy flux is sufficient to account for local auroral brightenings but is insufficient to account for the power typically associated with a substorm, which adds more weight that this phase is only pseudobreakup and is not substorm onset.

[52] The correlation of pseudobreakup, and earthward and tail moving flux ropes is not incidental. The causal relation between these processes is illustrated in Figure 9, which shows the evolution of the plasma pressure and proton temperature in the noon-midnight meridian and in the equatorial plane along with the nightside auroral currents. The development of the flux rope is associated with a local enhancement in total plasma pressure. At the first time shown there are two enhancements present: one moves tailward and expands in size, the other moves earthward

and intensifies but shrinks in vertical size. This change is consistent with the magnetic field features described above. The hottest particles are associated with the earthward moving flux rope and not the tailward moving flux rope. The energetic particles in the vicinity of the center of the flux rope appear to be swept up by the flux rope and pushed into the inner edge of the plasma sheet. These particles experience energization through adiabatic compression. The interaction of the earthward moving flux rope with the inner edge of the plasma sheet also produces acceleration of the plasma. This acceleration can be considered as either through increased  $J \times B$  acceleration produced by the superposition of the currents from the plasma sheet and flux rope piling up at the inner edge of the plasma sheet or by electric field acceleration driven by the rapid changes in the magnetic field previously described in association with breakup/onset.

[53] This energization produces energetic particle injection. The energetic particles can propagate along the field lines into the auroral regions, or expand around the flanks.

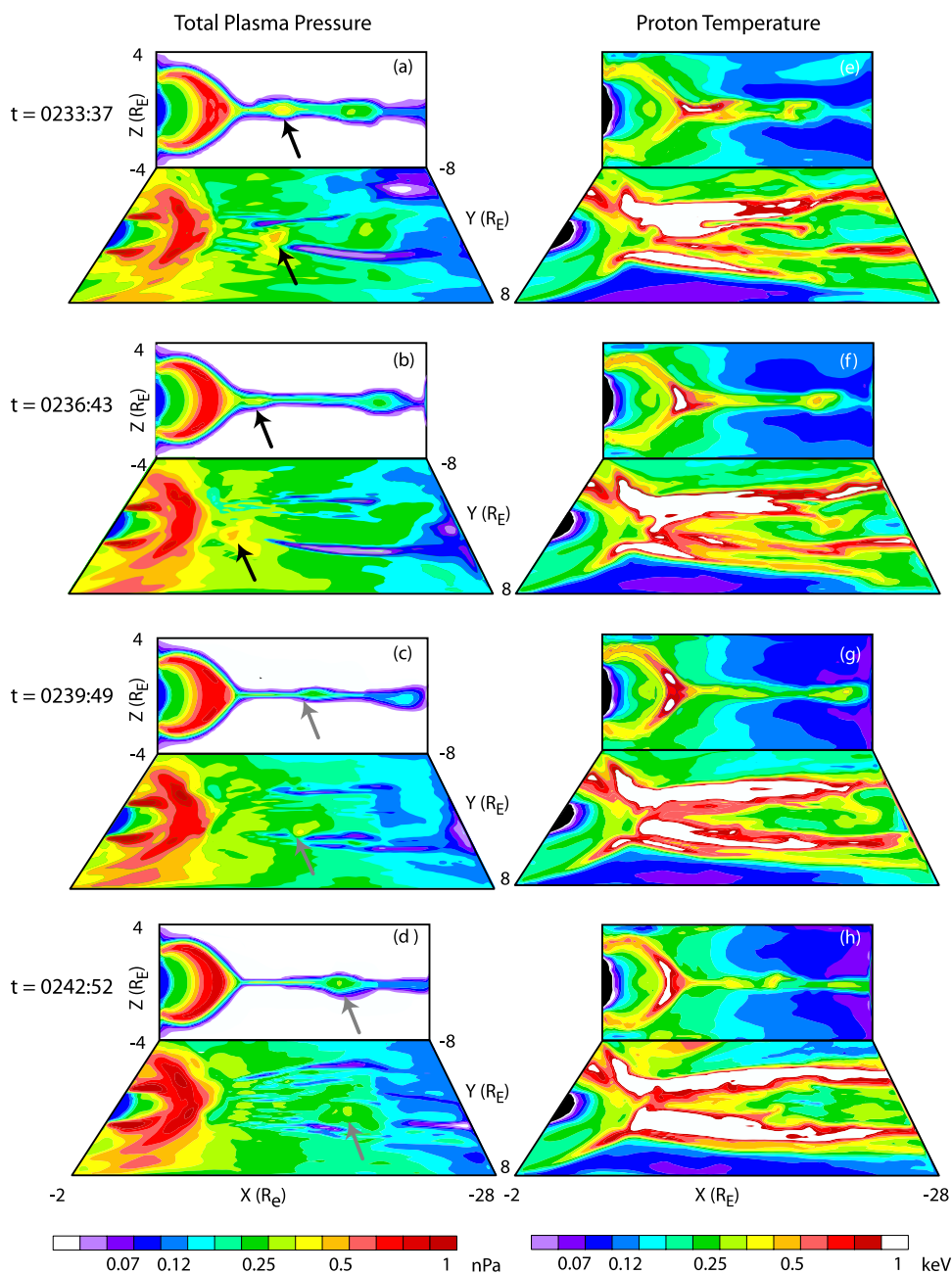


**Figure 9.** Evolution of (left) the total plasma pressure and (right) the proton temperature in the noon-midnight meridian and equatorial planes. The magnetic field lines out of the auroral zone follow the contours of the plasma pressure in the  $x$ - $z$  plane. The earthward moving flux rope is identified by a pressure maximum, as indicated by the black arrows, and is preceded and flanked by hot protons. The impact of the flux rope with the inner edge of the plasma sheet leads to the injection of hot particles up the auroral fields as well as around the dusk and dawn flanks. Reflection of some of the energy leads to the creation of a tailward moving flux rope as indicated by the gray arrows.

Both features are seen in Figure 9 and drive the auroral processes including the enhancement of the nightside auroral currents which are shown in Figure 10 corresponding to the times shown in Figure 9. The nightside auroral currents are seen to fully propagate around to the nightside by 0236:43, with its enhancement and poleward expansion associated with pseudobreakup occurring near 0239:49 UT. Note that because the inner boundary of the simulations is at

$2.7 R_E$  the timing of the auroral current intensification does not include the transit time over this later distance which would potentially add 1–2 min in the timing of the intensification.

[54] A third way that the plasma energy can be redistributed is through the partial reflection of energy off the inner edge of the plasma sheet back into the tail. Basically, there is an over compression of the magnetic fields and they

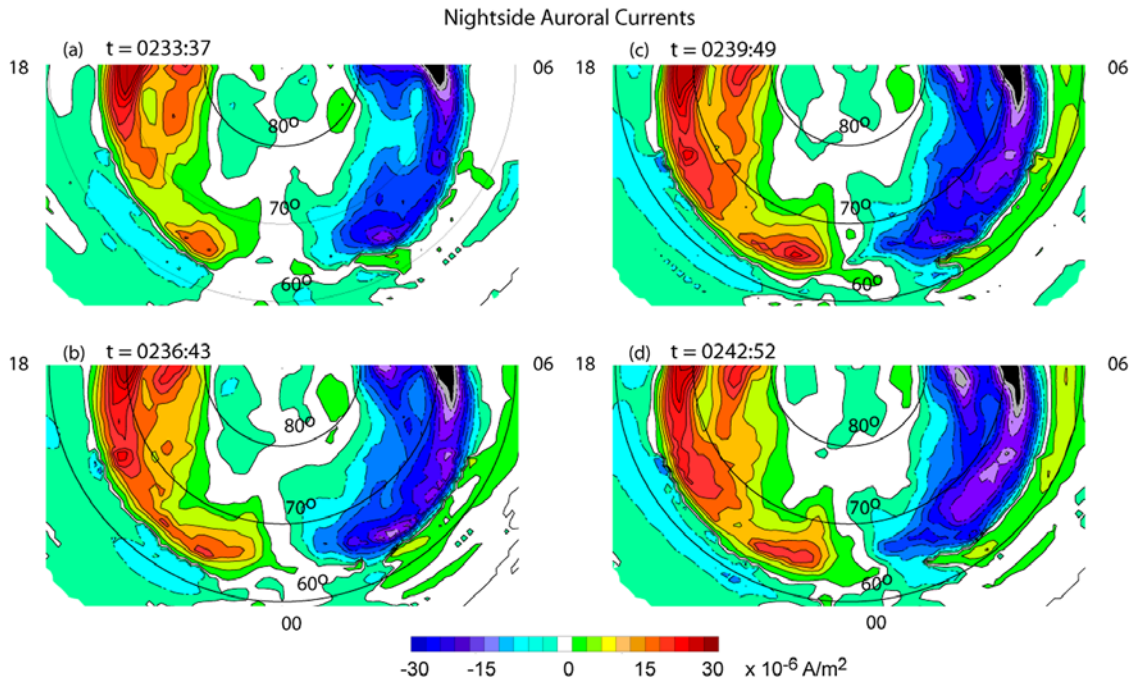


**Figure 10.** The evolution of the nightside auroral currents for the same times as in Figure 9. The arrival of the earthward moving flux rope at the inner edge of the plasma sheet coincides with increased current near midnight and expands poleward.

eventually recover leading to an outward pressure pulse. This partial reflection of energy is seen as the outward moving pressure feature seen in Figure 9d. This localized enhancement leads to the generation of the outward moving

flux rope in Figure 7. Thus, the earthward and tailward moving flux are not independent but are related. In addition, since the tailward moving flux ropes is embedded within plasma flows of 400 km/s this flux rope will catch up with

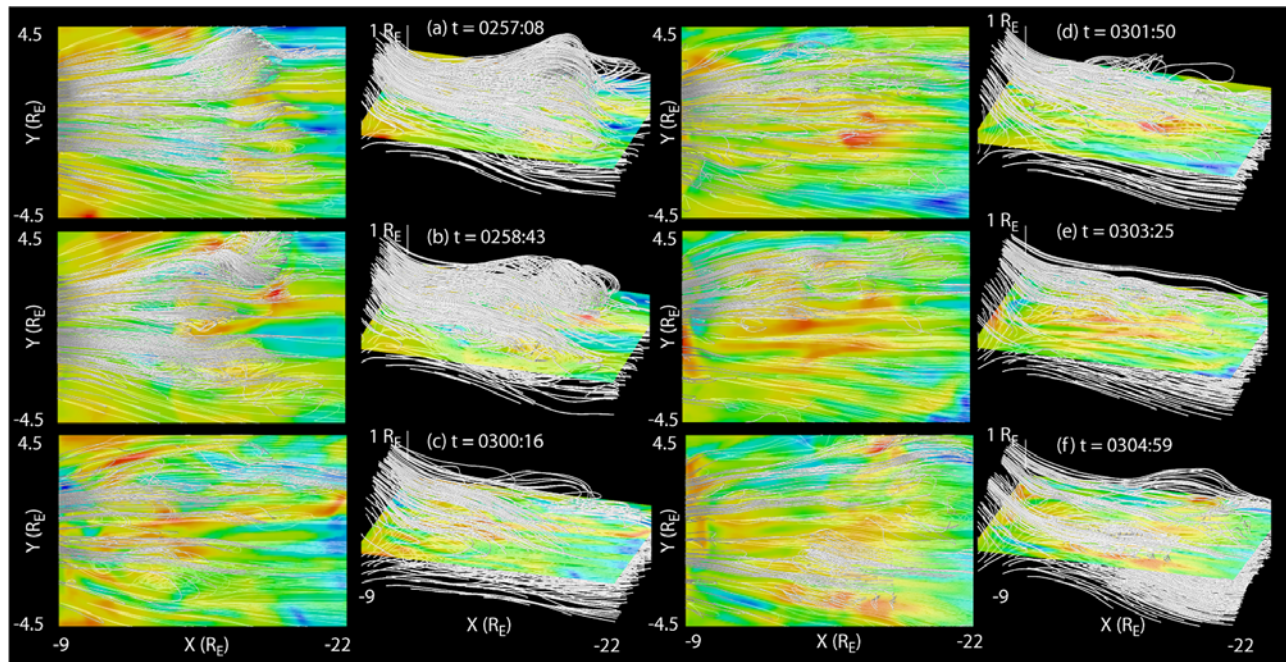


**Figure 11.** Continuation of Figure 7 showing the development of a second larger earthward moving flux rope that is followed by another tailward moving flux rope. The structure of earthward moving flux rope is dissipated when it impacts on the inner edge of the plasma sheet, which occurs at  $t = 0258:43$ .

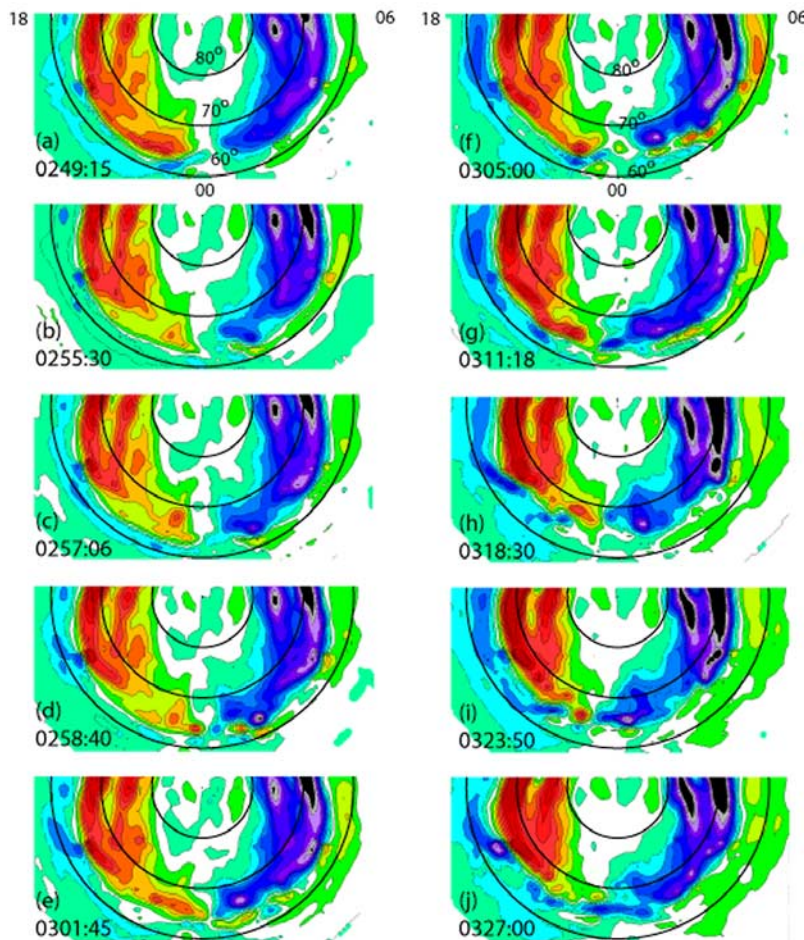


**Figure 12.** The evolution of the nightside currents covering the period shown in Figures 7 and 11. After the initial increase in the auroral currents produced by the first earthward moving flux rope, there is a decline in the nightside auroral currents between  $t = 0250$  and  $t = 0257$ . Onset associated with the arrival of the second earthward moving flux rope occurs at  $t = 0258:40$  with an intensification of the currents at midnight. Within a minute there is rapid propagation of the intensification both westward and eastward, though the westward intensifications are the strongest. Enhanced activity in the midnight sector continues for about 30 min.

the slower retreating X line. Since the tailward moving flux rope is on the earthward side of the X line it will experience a force toward the earth from the flows emanating from the X line. This means that energy from the tailward moving flux rope will be partially reflected earthward to aid in the generation of more intense earthward moving flux ropes. This partial energy reflection between the inner edge of the plasma sheet and the slow retreating X line provides an explanation of why there is an equal probability of observing earthward and tailward flux ropes.

## 5. Flux Ropes and Onset

[55] This tailward moving flux rope eventually interacts with the X line or earthward side of the plasmoid. This interaction can produce further acceleration and energization of plasma with partial reflection of energy back toward the earth.

[56] As a demonstration for this effect, Figure 11 shows that in the wake of this tailward moving flux rope a

earthward flux rope develops that is significantly larger than the earthward flux rope seen at pseudobreakup. This flux rope (Figure 11a) is at least twice the size in all directions to the first earthward flux rope in Figure 6. It again leads to fast dipolarization but over a more extended region over the tail (Figure 11c). There is also some reflection of energy back into the tail (Figure 11f).

[57] The corresponding auroral currents for the time periods in Figure 11 are shown in Figure 12. After the tailward flux rope has moved out of the region and before the arrival of the next earthward moving flux rope, the auroral currents are seen to decline relative to the currents in Figure 10. This creates a period of reduced activity of approximately 10 min, which is a well known occurrence before onset. Onset, as identified in section 4, is accompanied by a brightening near midnight at the equatorward edge at  $t = 0258:40$  (Figure 12d). The intensification then expands westward, as well as eastward (Figure 12e) on minute time scales. There is continued activity in this region until  $t = 0327$  (Figure 12j), producing some 30 min of

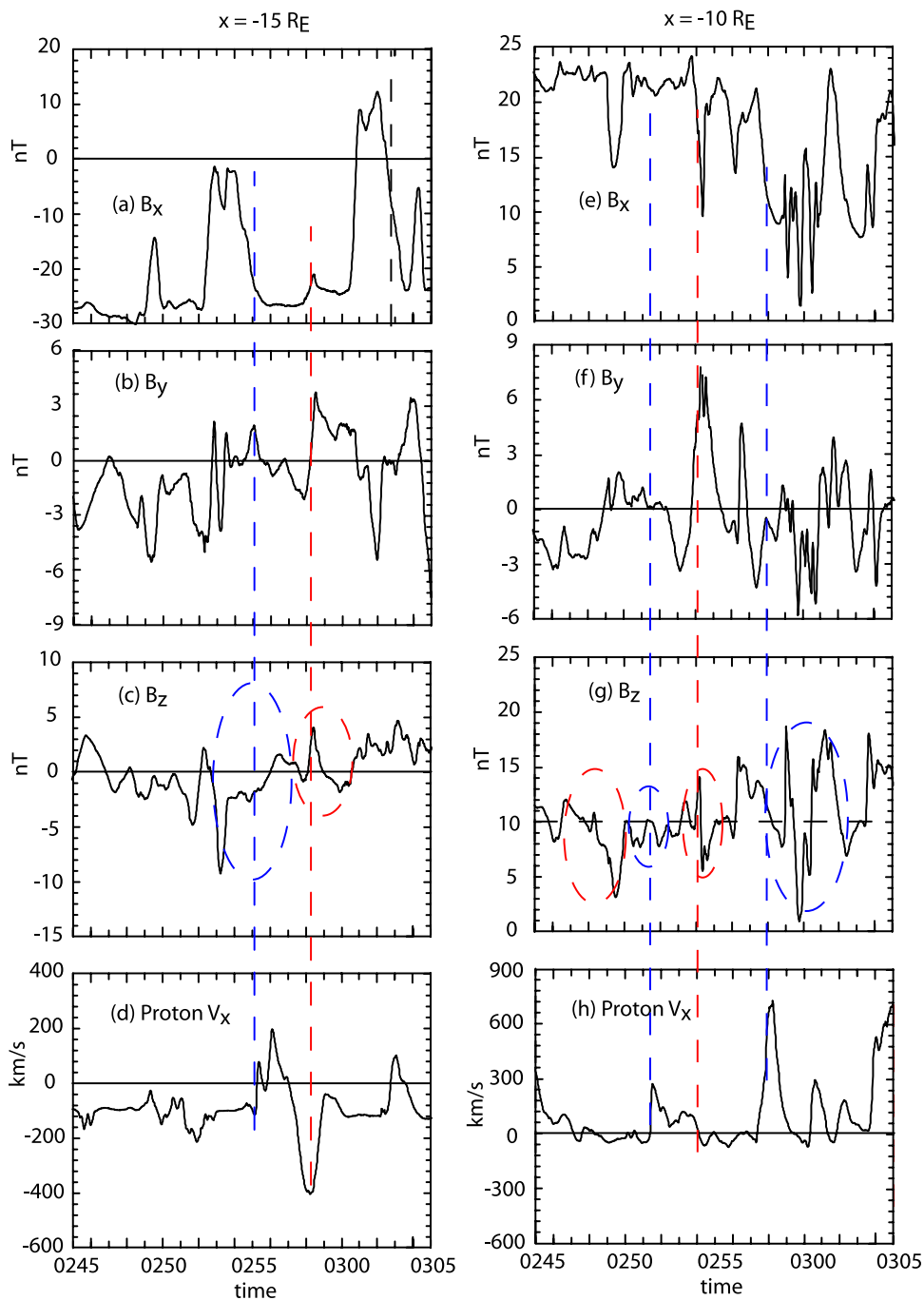


**Figure 13.** Time histories of  $B_x$ ,  $B_y$ ,  $B_z$ , and the proton  $V_x$  at (left)  $x = -15 R_E$  and (right)  $x = -10 R_E$  leading up to substorm onset. As in Figure 8 the earthward moving flux ropes are indicated by the blue dashed circles, and tailward moving flux ropes are indicated by the red dashed circles.

activity, which corresponds to the typical duration of an isolated substorm as noted in section 1.

[58] Thus, the one model appears to capture pseudo-breakup, a decrease in auroral activity 10 min prior to onset, rapid dipolarization associated with onset and a 30 min period for breakup. This model indicates that features of both NENL and CD models for substorms are in operation, but it is current disruption that occurs exactly at onset.

[59] It is important to note that substorm onset is not directly driven by reconnection itself. Reconnection signatures can be seen in the tail through the bulk of the growth phase. The plasma in the tail is under going increasingly stronger current sheet acceleration and the partial reflection of energy between the edge of the inner plasma sheet and the slow retreat X line adds to the buildup of the edge within the plasma sheet. This rapid deposition of energy due to the interaction of earthward moving flux ropes and the inner edge of the plasma sheet leads to a rapid modification of the

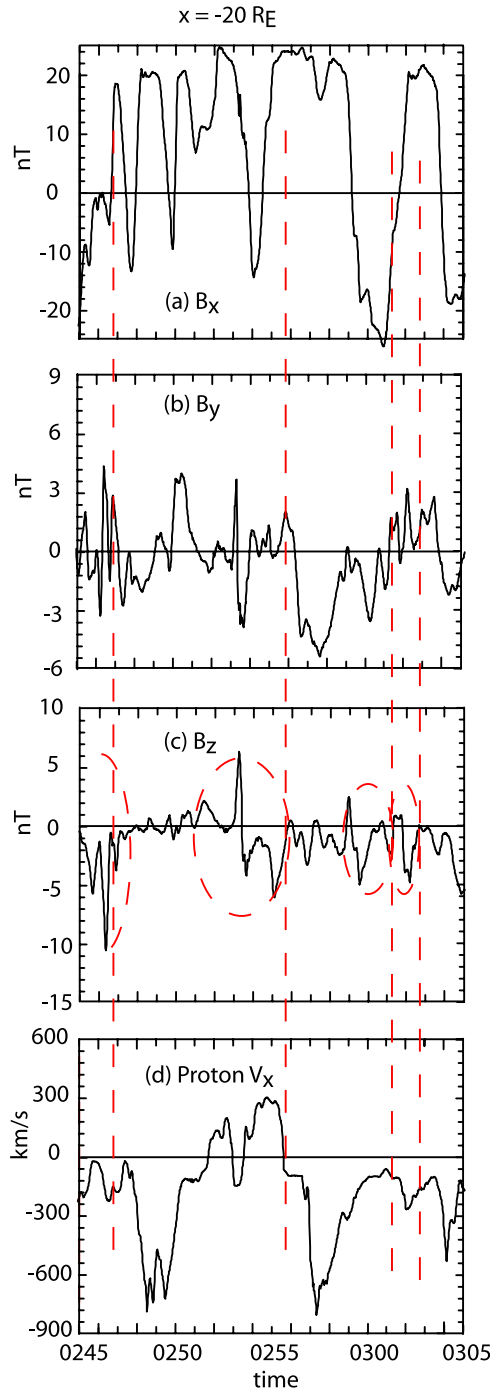


**Figure 14.** As in Figure 13 but at  $x = -20 R_E$  showing the predominance of tailward moving flux ropes and higher-frequency kinking of the tail up to substorm onset.

magnetic field and currents in the region which in turn lead to the intensification of the auroral current. Because the processes start at the inner edge of the plasma sheet the intensification of the nightside currents starts near the equatorward edge and expand poleward. This scenario for the initiation of the auroral enhancement more closely resembles the CD model for substorms and not the NENL model. Rapid dipolarization and further particle energization occurs because the  $B_z$  component of the magnetic field

on the earthward edge of the flux rope is opposite to the terrestrial magnetic field while the tailward edge of the flux rope leads to a more dipole-like configuration when added to the terrestrial magnetic field.

[60] The buildup of the energy in the flux ropes is illustrated in Figure 13 which shows the time history of the magnetic field and proton  $V_x$  at  $x = -15 R_E$  and  $-10 R_E$ . At both positions it is seen that the kinks in current sheet are become stronger with the perturbations in  $B_x$  increasing as substorm onset is approached. The spacecraft at  $x = -15 R_E$  actually temporarily crosses into the northern hemisphere (i.e.,  $B_x$  flips sign). Earthward moving flux ropes are identified by the blue circles ( $\mp B_z$ ) and tailward propagating flux ropes ( $\pm B_z$ ) by the red circles. Several of these flux ropes are associated with perturbations of the order of 10 nT compared with the 5 nT perturbations seen at pseudo-breakup (Figure 8). The speed of the tailward flux rope is about the same at about 400 km/s but the speed of the earthward moving flux ropes increase to above 600 km/s near the inner edge of the plasma sheet.

[61] The increase in speed and magnetic perturbations yields an increase in the energy flux of approximately 8 compared with that calculated in section 4 to yield energy densities of the order of  $40\text{--}80 \mu\text{J}/\text{m}^2/\text{s}$ . Taking into account the extra area of the flux rope, a total power of the order of 350 GW is available. This is a low estimate as we have yet to discuss the influence of heavy ions on the total dynamics. But 350 GW is of the correct order of magnitude to power a substorm.

[62] Figure 14 shows the corresponding magnetic perturbations and flow velocities further down the tail at  $x = -20 R_E$ . At this position, one sees small-scale kinking of the tail as seen by the oscillations in  $B_x$ . The period of these oscillations is as small as 3 min consistent with *Runov et al.* [2003] though their period appears to increase to about 6 min after substorm onset. These shorter-period oscillations are correlated with the highest  $V_y$  bulk velocities in  $O^+$  (section 6). At this distance down the tail, most of the flux ropes are propagating down the tail with speeds exceeding 600 km/s. These higher speeds are more typical of the tailward propagating flux ropes reported by *Slavin et al.* [2003a, 2003b]. Note that a strong flux rope signature is seen centered around 0255 UT just a few minutes before onset, similar to *Baker et al.* [2002] and *Angelopoulos et al.* [2008]. However, as we have demonstrated here it is inappropriate to identify this reconnection signature with causing substorm onset.

## 6. Fast Flows and Heavy Ion Influences

[63] There are two other influences that have potential on the development of substorms: bursty bulk flows and the presence of heavy ionospheric ions in the current sheet. We address both these issues in this section. Figure 15 shows the  $V_x$  component of the protons and  $O^+$  at the four sample positions shown in Figure 5. The characteristics of the velocity profiles are highly dependent on the position of the spacecraft. The solid line indicates the timing of the formation of the X line, and is well correlated with the development of fast tailward flows at  $x \sim 20 R_E$ . Because the sample point at  $x = -15 R_E$  is displaced  $0.5 R_E$  in  $z$  from the equator it primarily sees slower lobe flows, except after

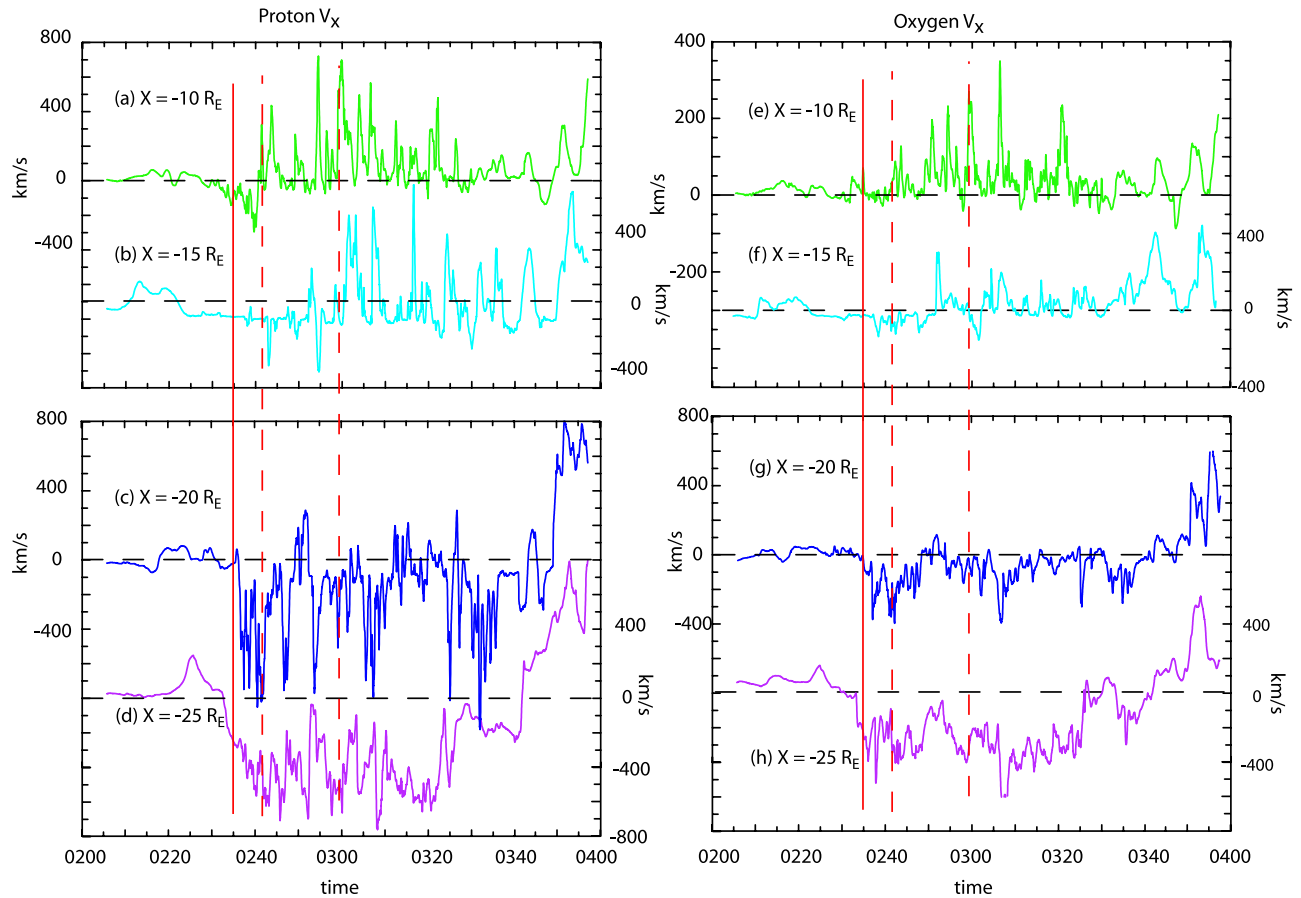


**Figure 15.** Evolution of (left) the proton and (right) the oxygen  $x$  component of the velocity at the four positions downtail used in Figure 5. The time of  $X$  line formation is indicated by the solid vertical line, and pseudobreakup and onset are indicated by the dashed vertical lines. The horizontal dashed lines give the zero for each of the graphs. Fast flows are seen down the tail in association with the formation of the  $X$  line. These flows develop several minutes before pseudobreakup and a few tens of minutes before onset. The protons have a speed that is on average twice that of the  $O^+$  ions in the Sun-Earth direction.

onset when bursty bulk flows toward the earth are observed. At the inner most point at  $x = -10 R_E$ , bursty bulk flows are seen much more often, even though the sample point has the same displacement away from the equatorial plane. This higher frequency occurs because of the vertical deflection of these flows as they approach the inner edge of the plasma sheet. In other words from the spacecraft perspective, the flows appear bursty but in fact that are present most of the time with the observed speed dependent on the position of the spacecraft from the center of the current sheet.

[64] Note that the bursty bulk flows at  $x = -10 R_E$  occur in association with pseudobreakup and onset (as indicated by the dashed lines), but fast flows can also be observed in this region in the absence of breakup. In other words, while fast flows are observed with pseudobreakup and onset, not all fast flows generate pseudobreakup and onset and as such it is the dissipation of the discrete bundle of plasma and magnetic field associated with the flux rope that generates pseudobreakup and onset, and bursty bulk flows by themselves are insufficient to cause onset.

[65] While  $V_x$  profiles for the  $O^+$  ions are very similar to the  $H^+$  profiles, an important difference is that the magnitude of  $V_x$  for the  $O^+$  ions is smaller by a factor of nearly

one half. The reason for this difference is that the heavy ions have a larger gyroradius and as such experience stronger dawn-dusk acceleration in the presence of a thin current sheet. This difference in acceleration is demonstrated in Figure 16 which shows the  $V_y$  component for the  $H^+$  and  $O^+$  ions. Beyond about  $x = -15 R_E$  the  $O^+$  ions have more than about twice the speed in the  $y$  direction as the  $H^+$  ions. This result is not new and is seen in single particle tracking results [Winglee, 2004]. What is new is that the current associated with the earthward moving flux ropes that appear at  $x = -15 R_E$  are strongly supported by the  $O^+$  ions while the  $H^+$  ions are supporting the bursty bulk flows.

[66] In the recent THEMIS substorm observations reported by Angelopoulos *et al.* [2008], the ion distribution had two discrete components: one was field aligned and one was propagating perpendicular to the magnetic field. The above results give a natural explanation for these features. The field-aligned component consists primarily of protons, and the perpendicular component is primarily  $O^+$ .

[67] A final question is whether ionospheric ions and in particular heavy ions are important for onset for an isolated substorm. As noted in section 1, the concentration of  $O^+$  for these events is typically much smaller than for storm time

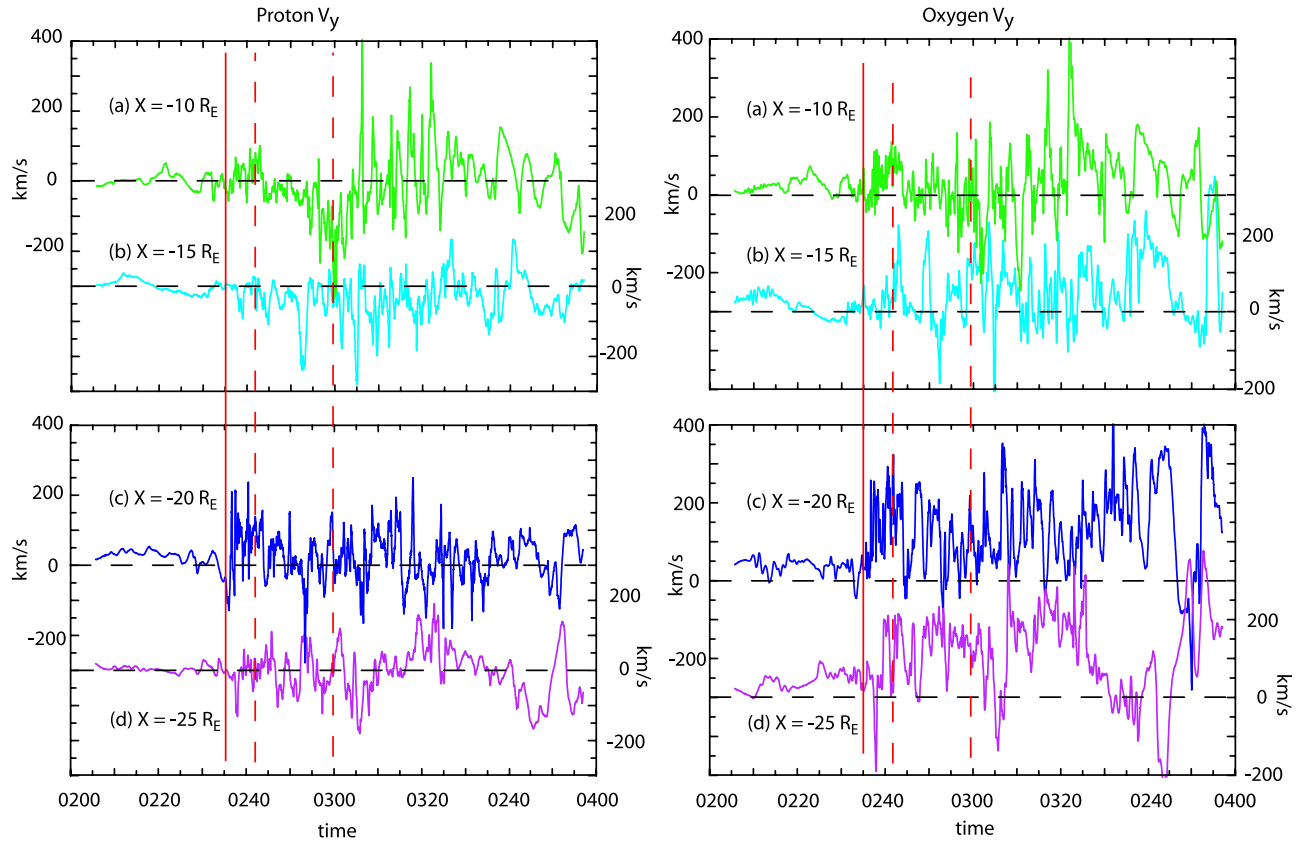


**Figure 16.** The evolution of  $V_y$  for  $H^+$  and  $O^+$  ions in the same format as Figure 15. In this case the  $O^+$  ions have the greatest speed in the dawn/dusk direction, indicating that they are important current carriers.

substorms [Korth *et al.*, 2002]. The general assumption is that the low concentration means  $O^+$  would only have limited impact on isolated substorm dynamics, with the influence of ionospheric  $H^+$  yet to be determined. The multifluid model provides direct insight into this question as shown in Figure 17, which shows the total plasma density, the relative densities of ionospheric  $H^+$  and  $O^+$  at 10 min intervals leading up to substorm onset. At the first time shown the density profile clearly shows a thin long current sheet associated with the formation of the Y line discussed in section 3. At this time the plasma sheet is primarily of solar wind origin through there is enhanced convection of ionospheric plasma in the lobes moving toward the plasma sheet. Because of the Y line structure of the plasma sheet, plasma is being convected either into the inner magnetosphere or down the tail, and as a result there is a monotonic decrease in the lobe and plasma sheet densities, with the lobe plasma feeding the plasma sheet. Because of these losses the relative importance of solar wind plasma declines, from being the dominant plasma at pseudobreakup ( $0230 < t < 0240$ ), to being the minority plasma component at substorm onset (at  $t = 0300$ ).

[68] The appearance of  $O^+$  is seen in Figure 17 to have a delayed response relative to the ionospheric  $H^+$  by an additional 10 min. It is only at  $t = 0300$  where there are sporadic increases in  $O^+$  and relative densities exceed 10% which is twice the assumed value at the ionospheric boundary conditions. Thus, there are enhanced levels of

$O^+$  in the plasma sheet at substorm onset, and as noted in Figure 16, these ions have a larger  $V_y$  than  $H^+$  and therefore at these concentrations they are able to support a significant amount of the cross-tail current. Thus, at least locally, ionospheric  $O^+$  ions are an important factor to substorm onset.

[69] The inhomogeneous nature of the  $O^+$  mass loading of the plasma sheet means that the amount of  $O^+$  that a spacecraft would observe is highly dependent on position with very low relative concentrations being present on the duskside of the plasma sheet, and maximum densities being present in the postmidnight sector. Thus, the lack of  $O^+$  in situ measurements cannot be used to rule out the influence of  $O^+$  on the tail dynamics during substorm onset. The inhomogeneous nature of the  $O^+$  mass loading is further illustrated in Figure 18 which shows the time profiles of the  $O^+$  relative density at the same locations are shown in Figure 17. The maximum concentration appears at  $15 R_E$  with significant  $O^+$  also being present at the inner edge of the plasma set and out to as far as about  $20 R_E$ . As noted earlier, this region is where the flux ropes, both earthward and tailward propagating, first appear. As such, the role of  $O^+$  with respect to substorm onset cannot be neglected.

[70] The participation of  $O^+$  in the tail dynamics at substorm onset is shown in Figure 19, which shows cuts of the  $O^+$  pressure (contours) and velocity (arrows) in the tail. The flux rope that initiates substorm onset is seen as the large enhancement in pressure intensity and width of the

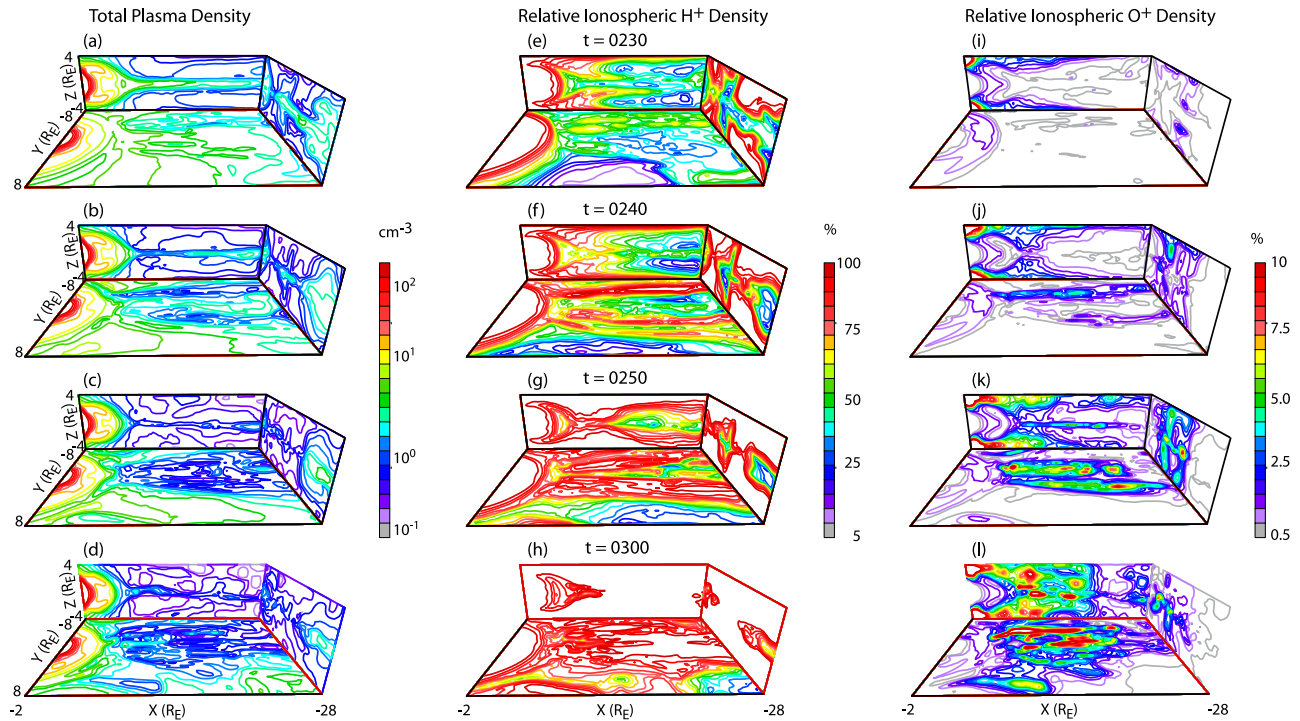


**Figure 17.** Evolution of the (left) total plasma density, (middle) relative ionospheric  $H^+$  density, and (right) relative  $O^+$  density in the noon-midnight meridian, equatorial plane, and across the tail at  $x = -20 R_E$ . The latter is displaced to the right so that the other two views are not obscured. During X line formation, the solar wind plasma dominates the plasma sheet composition. This composition changes to being dominated by ionospheric  $H^+$  around the time of pseudobreakup, with  $O^+$  being a significant factor at substorm onset.

plasma sheet at  $t = 0258:38$ . As this flux rope moves inward, there is enhanced flow of plasma from the lobes into the sheet. This is seen as an increase in the vertical speed in the noon-midnight meridian, and preferentially adds  $O^+$  plasma into the flux rope and in its wakes. This enhancement in  $V_z$  starts at 0257:04 (Figure 19b) and continues until 0303:24 (Figure 19f). As the  $O^+$  convects into the rear of the flux rope and current sheet, it is further energized so that the contribution of  $O^+$  to these regions is greatly enhanced (as in Figure 19c). This  $O^+$  enriched plasma is delivered to the inner edge of the plasma and as such will participate in the disruption of the inner edge of the plasma sheet. Thus, while  $O^+$  does not initiate the generation of the flux ropes,  $O^+$  can be enriched within them because of propagation effects, and with this enrichment they can significantly contribute to the total energy being deposited to the inner edge of the plasma sheet. In addition because of their relatively large gyroradius and period, they can experience stronger acceleration that protons in the fast varying electric and magnetic fields associated with dipolarization. This energization of these heavy ions at the inner edge of the plasma sheet would lead to the heavy ions being an important contributor to substorm injection and the generation of the partial ring current.

[71] Another feature seen in Figure 19 is the tail kinking (as seen in the cross-tail cuts) with vertical displacements of about  $0.5$  to  $1 R_E$  for the solar wind conditions considered here. This kinking can lead to the apparent multiple crossing of the current sheet by a slow moving spacecraft as seen by

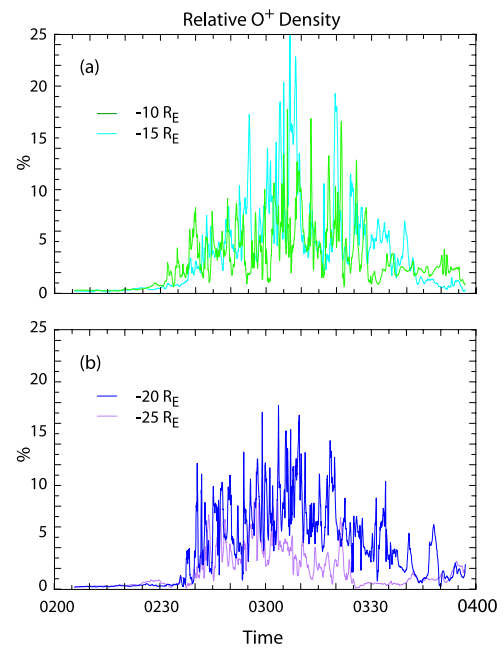


**Figure 18.** The temporal evolution of the relative  $O^+$  density. Shortly after the formation of the X line, there are enhancements in the  $O^+$  density at  $x \geq -20 R_E$ , where the flux ropes develop.

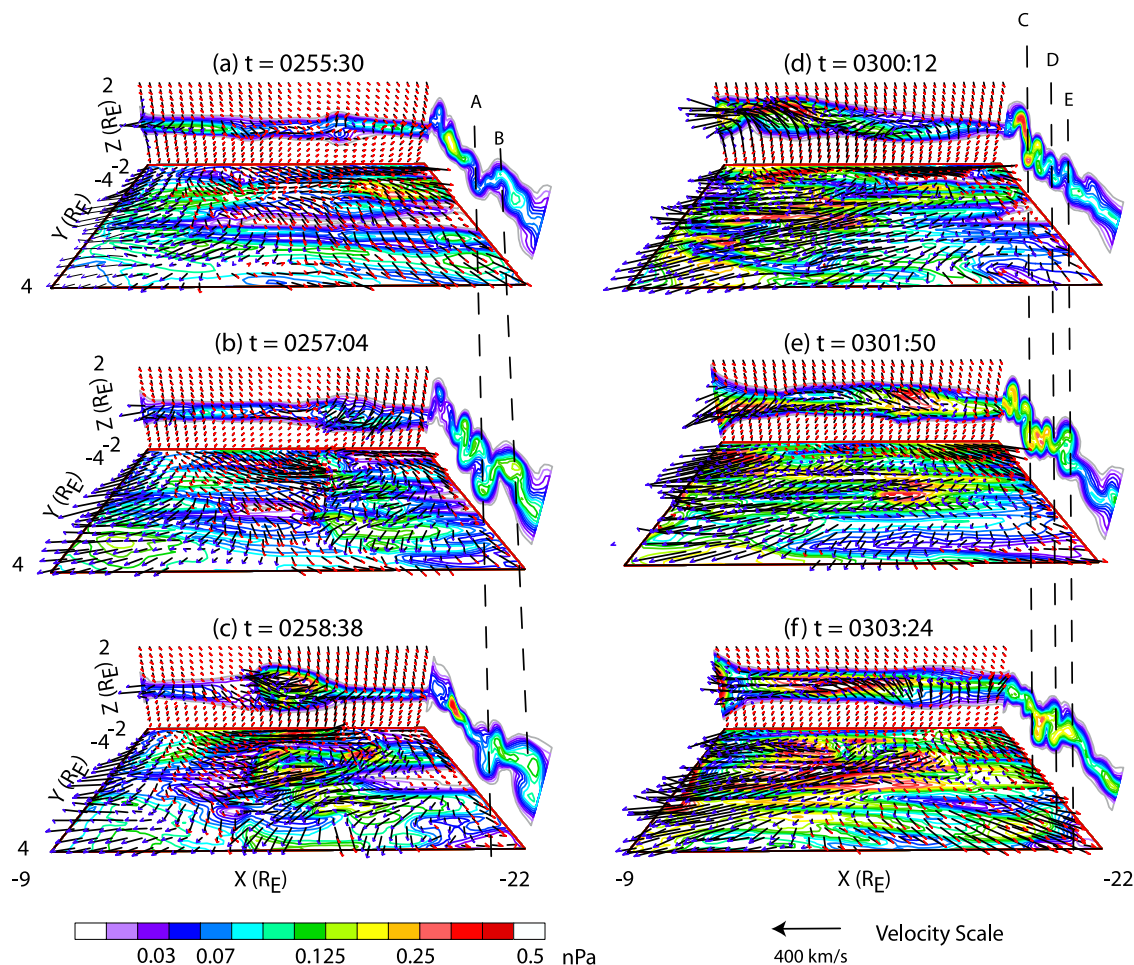


**Figure 19.** Evolution of the  $O^+$  pressure (contours) and velocity (arrows) during the development of the earthward moving flux rope that produces substorm onset. Red-tipped arrows indicate tailward flow, whereas blue-tipped arrows indicate earthward flow. The passage of the earthward moving flux rope (which is seen as a bulge in the plasma pressure) leads to enhanced  $O^+$  contributions to the overall pressure in the plasma sheet, so that  $O^+$  has a nonnegligible contribution to onset. The black dashed lines show the propagation and evolution of the kinks as they move in the dawn-to-dusk direction.

fast flips in the sign of  $B_x$ , as previously mentioned in sections 3 and 4. There are different inherent scale sizes for the wavelength of the kinks in the  $y$  direction. The larger of the scale sizes has wavelength of about  $4 R_E$  (e.g., Figure 14a) and this large-scale length appears to be associated with inhomogeneous mass loading from the ionosphere. On these scale sizes the plasma can have significantly different path lengths and propagation times to reach the plasma sheet. The resultant time lag to responses to the solar wind conditions then leads to large-scale warping of the plasma sheet.

[72] Imposed on this large-scale size are smaller-scale size ( $0.25$ – $0.5 R_E$ ) kinks which are very prominent in Figures 19b, 19d, and 19f. These kinks propagate both along the Sun-Earth line as well as across the tail as indicated by the dashed vertical lines. This cross-tail propagation is seen with the larger of the kinks in Figure 19a moving toward dusk in Figures 19b and 19c and similarly between Figures 19d–19f, as indicated by the dashed lines. On average they have a speed of about  $150$  km/s in the

dawn dusk direction. The wavelength of these kinks is of the order of an  $O^+$  gyroradius, at  $1000$ – $2000$  km. This scale size and the propagation of the kinks are consistent with that reported from Cluster observations [e.g., Runov *et al.*, 2006]. Note though that close inspection of the kinks shows that some of the kinks that develop on the dawnside can propagate toward dawn. Runov *et al.* [2006] did not observe any such propagation, but this may be due to the restricted position of the spacecraft during the event.

[73] In addition, as demonstrated above the  $O^+$  ions have the largest drift velocity in the  $y$  direction, and therefore drive the cross-tail propagation of the kinks. Additional evidence for this is that small-scale kinks have the shortest wavelengths when  $V_y$  of the  $O^+$  ions is small and increases with this velocity component. This correlation suggests that  $O^+$  has a major role in the development of the small-scale kinks, though the complexity of the tail dynamics prevents a definitive causal relation to be established. It is important to note that these kinks are seen to become nonlinear where they interact with each other (Figures 19d and 19f) and as

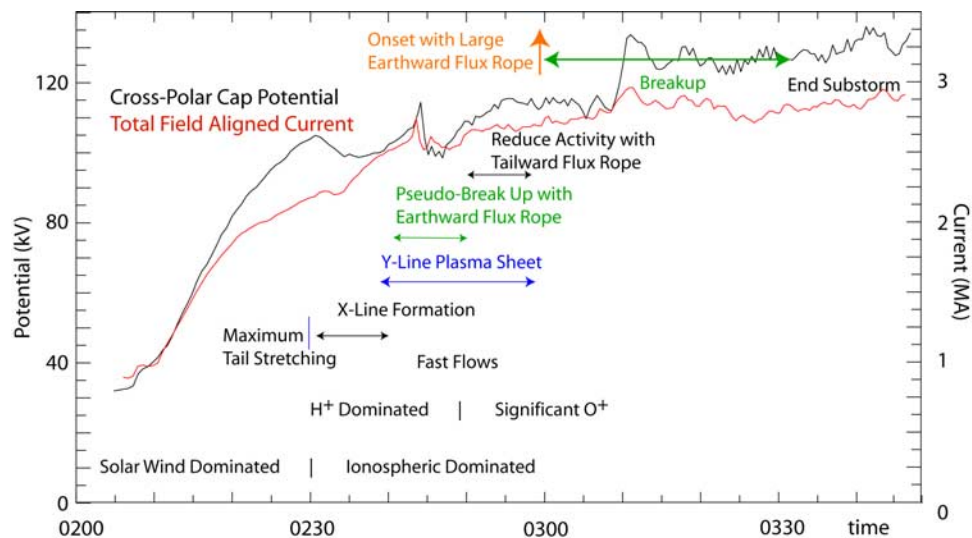


**Figure 20.** The timing of processes that lead up to onset and breakup for an isolated internally triggered substorm relative to the development of the cross-polar cap potential (black line) and total integrated upward current out of the northern hemisphere. X line reconnection occurs at about the time that the cross-polar cap potential and field aligned currents saturate. At this time the solar wind is the dominant contributor to the plasma in the plasma sheet. Pseudobreakup occurs in association with an earthward moving flux rope impacting the inner edge of the plasma sheet, with continued activity occurring as a tailward flux rope is induced by reflected energy. A period of relative quiet develops in the absence of any flux ropes. Ionospheric plasma starts to become the dominant source of plasma in the plasma sheet. A large-scale earthward moving flux rope generates onset with rapid dipolarization and enhancement of the nightside auroral currents.

such add to the dissipation processes within the plasma sheet. So while  $O^+$  may be late for pseudobreakup, it is actively involved in substorm onset, and the continuing activity seen in association with breakup.

## 7. Summary and Conclusions

[74] This paper examines the interplay of large- and small-scale processes in association with the development of substorm onset. Within a thin current sheet a simple dimensional analysis shows that ion skin and ion gyroradius effects must be important in fully describing their dynamics. These effects are neglected in MHD but are included in the multifluid/multiscale methodology which is used to demonstrate the importance of these effects at both small and large scales within global magnetosphere.

[75] The results presented here shows that the above small-scale processes have major impact on the global dynamics. However, the reverse is also true. Studying small-scale processes without an understanding of the global dynamics can lead to an oversimplified or possibly an overly restrictive image of the dynamics of the system. The case in point is the controversy between the NENL and CD models for substorms. The NENL relies entirely on reconnection processes to produce substorm onset. The problem with this hypothesis is that the reconnection is occurring at distances thought to be very far from the point of origin of the auroral brightenings associated with substorm onset. The CD model is able to account for the latter but is unable to place the current disruption into the context

of well-documented reconnection signatures including plasmoids and flux ropes.

[76] The multifluid/multiscale model is able to account for multiple substorm features and indicates that a combination of the CD and NENL models actually leads to the most accurate description of an isolated substorm. The exact timing of different processes is dependent on the initial configuration of the magnetosphere. In the present case we have taken a mildly active system where the IMF is initially zero (as opposed to a quiet magnetosphere where the IMF has been northward for an extended period).

[77] The timing of substorm processes is summarized in Figure 20 and shown schematically in Figure 21. These processes are as follows.

[78] 1. IMF turns southward leading to intensifications of the auroral currents and cross-polar cap potential reaching approximate saturation within 30 min.

[79] 2. In this first 30 min the solar wind is the dominant plasma species in the plasma sheet.

[80] 3. At the end of this 30 min, the field lines in the inner magnetosphere have reached maximum stretching and an X line forms.

[81] 4. A large plasmoid is ejected and the X line begins to move tailward within about 10 min after its formation.

[82] 5. Ionospheric light ions start to become the dominant ion species at this time.

[83] 6. With the tailward motion of the X line, a thin current sheet ( $\sim 400$  km) forms causing the tail to have a Y line structure.

[84] 7. Fast flows develop in the tail, and localized pinching of the thin current sheet leads to the generation

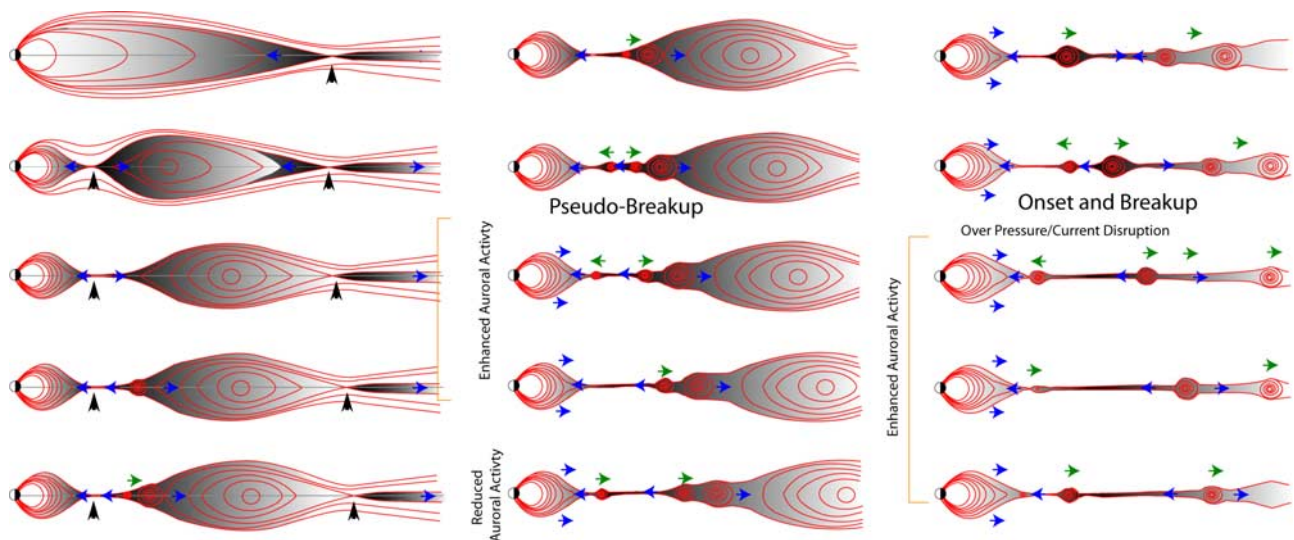


**Figure 21.** A schematic showing the development of substorms that summarizes the processes in Figure 20. Black arrows indicate position of X lines, blue arrows indicate the flow of plasma, and green arrows indicate the flow direction of flux ropes. The first half of the growth phase is identical to the NENL [Hones, 1984]. The schematic differs after the ejection of the plasmoid with the formation of a Y line in which small-scale flux ropes develop in the wake of the plasmoid. The arrival of a small earthward moving flux rope at the inner edge of the plasma sheet produces a pseudobreakup. The reflected edge can drive a tailward flux rope, and its interaction with the retreating X line can lead to a larger-scale earthward moving flux rope that generates substorm onset when it impacts on the inner edge of the plasma sheet.

of flux ropes. Some of these flux ropes propagate tailward while others propagate earthward.

[85] 8. The fast flows can have two components: a fast field-aligned proton component and a cross-tail component comprising mainly  $O^+$ .

[86] 9. Dissipation of a small earthward moving flux rope of the inner edge of the plasma sheet leads to pseudobreakup, including short-duration enhancements in the nightside auroral currents, and short-lived dipolarization near the inner edge of the plasma sheet.

[87] 10. Partial reflection of energy from the earthward moving flux rope can lead to the generation of a tailward moving flux rope.

[88] 11. After this period and before the arrival of the next earthward moving flux rope there is a period of approximately 10 min where there is declining auroral activity.

[89] 12. This tailward moving flux rope can interact with the retreating X line that leads to a larger-scale earthward moving flux rope.

[90] 13. This bigger earthward moving flux rope draws more  $O^+$  inner the plasma sheet whether there is additional energization of  $O^+$  so that locally it can be a very important aspect substorm onset.

[91] 14. Strong kinking of the plasma sheet occurs at this time so that a spacecraft near the equator will experience multiple crossings between southern and northern hemispheres.

[92] 15. This earthward moving flux rope then dissipates on the inner edge of the plasma sheet, leading to substorm onset as seen by a fast (1 min) dipolarization, enhancement of the nightside auroral currents and magnetospheric injection of energetic particles.

[93] 16. Dissipation of the energy deposited at the inner edge of the plasma sheet leads to breakup that lasts for about 30 min.

[94] The first part of the scenario derived from the present work as shown in Figure 21 is very close to the NENL model. However, we assert that X line reconnection is not the trigger for substorm onset. It is the discrete transfer of energy from the thin current sheet that forms in the wake of the X line that is the true driver for substorm onset, with the deposition of its energy onto the inner edge of the plasma sheet and the resultant rapid changes in the magnetic field there that produces substorm onset. In this manner the modeling indicates that the CD model gives the most accurate description of the processes that produce substorm onset.

[95] The scenario outlined above ties many observations, including timing of reconnection signatures, inner edge of the plasma sheet, flux ropes, fast flows and ionospheric plasma in the plasma sheet into one single unifying model. It is able to do so because it ties small- and large-scale processes into a single model. It provides the physical link that has been disputed between CD and NENL models of substorms. Additionally, the inner edge of the plasma sheet and the X line are not independent features of the tail, but in fact there is coupling between the two regions as they provide mirrors reflecting energy between them.

[96] Further work needs to validate the predictions made here, but the fact that so many different pieces appear to fit into the one model is very encouraging. One important caveat to our conclusions is that all the processes derived are for an internally driven substorm where the IMF is

constant and southward. A follow-up paper will examine externally driven substorms where the IMF becomes more northerly. The scenario for externally triggered substorms is essentially the same as described here except that solar wind plasma plays a greater role and  $O^+$  potentially a smaller role.

[97] **Acknowledgments.** This work was supported by NASA grants NNX08A067G and NNX07APGGC and NSF grant ATM 0617654 to the University of Washington.

[98] Amitava Bhattacharjee thanks the reviewers for their assistance in evaluating this paper.

## References

- Akasofu, S.-I. (1964), The development of the auroral substorm, *Planet. Space Sci.*, *12*, 273, doi:10.1016/0032-0633(64)90151-5.
- Angelopoulos, V., W. Baumjohann, C. F. Kennel, F. V. Coroniti, M. G. Kivelson, R. Pellat, R. J. Walker, H. Lühr, and G. Paschmann (1992), Bursty bulk flows in the inner central plasma sheet, *J. Geophys. Res.*, *97*, 4027, doi:10.1029/91JA02701.
- Angelopoulos, V., F. S. Mozer, T. Mukai, K. Tsuruda, S. Kokubun, and T. J. Hughes (1999), On the relationship between bursty bulk flows, current disruption and substorms, *Geophys. Res. Lett.*, *26*, 2841, doi:10.1029/1999GL00601.
- Angelopoulos, V., et al. (2008), Tail reconnection triggering substorm onset, *Science*, *321*, 931, doi:10.1126/science.1160495.
- Arnoldy, R. L., and K. W. Chan (1969), Particle substorms observed at the geostationary orbit, *J. Geophys. Res.*, *74*, 5019, doi:10.1029/JA074i021p05019.
- Baker, D. N., T. I. Pulkkinen, V. Angelopoulos, W. Baumjohann, and R. L. McPherron (1996), Neutral line model of substorms: Past results and present view, *J. Geophys. Res.*, *101*, 12,975, doi:10.1029/95JA03753.
- Baker, D. N., et al. (2002), Timing of magnetic reconnection initiation during a global magnetospheric substorm onset, *Geophys. Res. Lett.*, *29*(24), 2190, doi:10.1029/2002GL015539.
- Baumjohann, W., G. Paschmann, and H. Lühr (1990), Characteristics of high-speed ion flows in the plasma sheet, *J. Geophys. Res.*, *95*, 3801, doi:10.1029/JA095iA04p03801.
- Eastwood, J. P., D. G. Sibeck, J. A. Slavin, M. L. Goldstein, B. Lavraud, M. Sitnov, S. Imber, A. Balogh, E. A. Lucek, and I. Dandouras (2005), Observations of multiple X-line structure in the Earth's magnetotail current sheet: A Cluster case study, *Geophys. Res. Lett.*, *32*, L11105, doi:10.1029/2005GL022509.
- Elphic, R. C., C. A. Cattell, K. Takahashi, S. J. Bame, and C. T. Russell (1986), ISEE-1 and 2 observations of magnetic flux ropes in the magnetotail: FTE's in the plasma sheet?, *Geophys. Res. Lett.*, *13*, 648, doi:10.1029/GL013i007p00648.
- Elphic, R. C., et al. (1998), The auroral current circuit and field-aligned currents observed by FAST, *Geophys. Res. Lett.*, *25*, 2033, doi:10.1029/98GL01158.
- Feldstein, Y. I., and Y. I. Galperin (1985), The auroral luminosity structure in the high-latitude upper atmosphere: Its dynamics and relationship to the large-scale structure of the Earth's magnetosphere, *Rev. Geophys.*, *23*, 217, doi:10.1029/RG023i003p00217.
- Harnett, E. M., and R. M. Winglee (2003), 2.5-D fluid simulations of the solar wind interacting with multiple dipoles on the surface of the Moon, *J. Geophys. Res.*, *108*(A2), 1088, doi:10.1029/2002JA009617.
- Harnett, E. M., and R. M. Winglee (2007), High-resolution multifluid simulations of the plasma environment near the Martian magnetic anomalies, *J. Geophys. Res.*, *112*, A05207, doi:10.1029/2006JA012001.
- Harnett, E. M., R. M. Winglee, and P. A. Delamere (2005), Three-dimensional multi-fluid simulations of Pluto's magnetosphere: A comparison to 3D hybrid simulations, *Geophys. Res. Lett.*, *32*, L19104, doi:10.1029/2005GL023178.
- Harnett, E. M., R. M. Winglee, and C. Paty (2006), Multi-scale/multi-fluid simulations of the post plasmoid current sheet in the terrestrial magnetosphere, *Geophys. Res. Lett.*, *33*, L21110, doi:10.1029/2006GL027376.
- Harnett, E. M., R. M. Winglee, A. Stickle, and G. Lu (2008), Prompt ionospheric/magnetospheric responses 29 October 2003 Halloween storm: Outflow and energization, *J. Geophys. Res.*, *113*, A06209, doi:10.1029/2007JA012810.
- Henderson, M. G., G. D. Reeves, R. D. Belian, and J. S. Murphree (1996), Observations of magnetospheric substorms occurring with no apparent solar wind/IMF trigger, *J. Geophys. Res.*, *101*, 10,773, doi:10.1029/96JA00186.
- Hones, E. W., Jr. (1984), Plasma sheet behavior during substorms, in *Magnetic Reconnection in Space and Laboratory Plasmas*, *Geophys. Monogr. Ser.*, vol. 30, edited by E. W. Hones Jr., p. 178AGU, Washington, D. C.
- Horwitz, J. L. (1985), The substorm as an internal magnetospheric instability: Substorms and their characteristic timescales during intervals of steady interplanetary magnetic field, *J. Geophys. Res.*, *90*, 4146.
- Kan, J. R. (1998), A globally integrated substorm model: Tail reconnection and magnetosphere-ionosphere coupling, *J. Geophys. Res.*, *103*, 11,787, doi:10.1029/98JA00361.
- Kelley, M. C. (1989), *The Earth's Ionosphere: Plasma Physics and Electrodynamics*, Academic, New York.
- Kennel, C. F. (1992), The Kiruna conjecture: The strong version, in *Substorms 1: Proceedings of the First International Conference on Substorms*, edited by C. Mattok, *Eur. Space Agency Spec. Publ.*, *ESA-SP 335*, 599.
- Kistler, L. M., et al. (2005), Contribution of nonadiabatic ions to the cross-tail current in an  $O^+$  dominated thin current sheet, *J. Geophys. Res.*, *110*, A06213, doi:10.1029/2004JA010653.
- Kokubun, S., and R. L. McPherron (1981), Substorm signatures at synchronous altitude, *J. Geophys. Res.*, *86*, 11,265, doi:10.1029/JA086iA13p11265.
- Korth, A., R. H. W. Friedel, F. Frutos-Alfaro, C. G. Mouikis, and Q. Zong (2002), Ion composition of substorms during storm-time and non-storm-time periods, *J. Atmos. Sol. Terr. Phys.*, *64*, 561, doi:10.1016/S1364-6826(02)00013-5.
- Krall, N. A., and A. W. Trivelpiece (1972), *Principles of Plasma Physics*, 119 pp., McGraw-Hill, New York.
- Le, G., G. Lu, R. J. Strangeway, and R. F. Pfaff Jr. (2002), Strong interplanetary magnetic field  $B_y$ -related plasma convection in the ionosphere and cusp field-aligned currents under northward interplanetary magnetic field conditions, *J. Geophys. Res.*, *107*(A12), 1477, doi:10.1029/2001JA007546.
- Lepping, R. P., D. H. Fairfield, J. Jones, L. A. Frank, W. R. Paterson, S. Kokubun, and T. Yamamoto (1995), Cross-tail magnetic flux ropes as observed by the GEOTAIL spacecraft, *Geophys. Res. Lett.*, *22*, 1193.
- Lepping, R. P., J. A. Slavin, M. Hesse, J. A. Jones, and A. Szabo (1996), Analysis of magnetotail flux ropes with strong core fields: ISEE 3 observations, *J. Geomag. Geoelectr.*, *48*, 589.
- Li, Q., R. M. Winglee, M. Wilber, L. Chen, and G. Parks (2000), The geopause in relation to the plasma sheet and the low-latitude boundary layer: Comparison between Wind observations and multifluid simulations, *J. Geophys. Res.*, *105*, 2563, doi:10.1029/1999JA900369.
- Liou, K., C.-I. Meng, A. T. Y. Lui, P. T. Newell, and S. Wing (2002), Magnetic dipolarization with substorm expansion onset, *J. Geophys. Res.*, *107*(A7), 1131, doi:10.1029/2001JA000179.
- Lopez, R. E., H. Lühr, B. J. Anderson, P. T. Newell, and R. W. McEntire (1990), Multipoint observations of a small substorm, *J. Geophys. Res.*, *95*, 18,897, doi:10.1029/JA095iA11p18897.
- Lui, A. T. Y. (1991), A synthesis of magnetospheric substorm models, *J. Geophys. Res.*, *96*, 1849.
- Lui, A. T. Y. (1996), Current disruption in the Earth's magnetosphere: Observations and models, *J. Geophys. Res.*, *101*, 13,067, doi:10.1029/96JA00079.
- Lui, A. T. Y. (2004), Potential plasma instabilities for substorm expansion onset, *Space Sci. Rev.*, *113*, 127, doi:10.1023/B:SPAC.0000042942.00362.4e.
- Lui, A. T. Y., R. E. Lopez, B. J. Anderson, K. Takahashi, L. J. Zanetti, R. W. McEntire, T. A. Potemra, D. M. Klumppar, E. M. Greene, and R. Strangeway (1992), Current disruptions in the near-Earth neutral sheet region, *J. Geophys. Res.*, *97*, 1461, doi:10.1029/91JA02401.
- Lyons, L. R., G. T. Blanchard, J. C. Samson, R. P. Lepping, T. Yamamoto, and T. Moretto (1997), Coordinated observations demonstrating external substorm triggering, *J. Geophys. Res.*, *102*, 27,039, doi:10.1029/97JA02639.
- McIlwain, C. E. (1974), Substorm injection boundaries, in *Magnetospheric Physics*, edited by B. M. McCormac, p. 143, D. Reidel, Norwell, Mass.
- McIlwain, C. E. (1992), Auroral mapping during substorms, in *Substorms 1: Proceedings of the First International Conference on Substorms*, edited by C. Mattok, *Eur. Space Agency Spec. Publ.*, *ESA-SP 335*, 65.
- McPherron, R. L. (1970), Growth phase of magnetospheric substorms, *J. Geophys. Res.*, *75*, 5592, doi:10.1029/JA075i028p05592.
- Meng, C.-I., and K. Liou (2004), Substorm timings and time scales: A new aspect, *Space Sci. Rev.*, *113*, 41, doi:10.1023/B:SPAC.0000042939.88548.68.
- Moldwin, M. B., and W. J. Hughes (1991), Plasmoids as magnetic flux ropes, *J. Geophys. Res.*, *96*, 14,051, doi:10.1029/91JA01167.
- Moldwin, M. B., and W. J. Hughes (1992), Plasmoid observations in the distant plasma sheet boundary layer, *Geophys. Res. Lett.*, *19*, 1911, doi:10.1029/92GL02102.
- Nagai, T., M. Fujimoto, Y. Saito, S. Machida, T. Terasawa, R. Nakamura, T. Yamamoto, T. Mukai, A. Nishida, and S. Kokubun (1998), Structure and dynamics of magnetic reconnection for substorm onsets with Geotail observations, *J. Geophys. Res.*, *103*, 4419.
- Nagai, T., I. Shinohara, M. Fujimoto, S. Machida, R. Nakamura, Y. Saito, and T. Mukai (2003), Structure of the Hall current system in the

- vicinity of the magnetic reconnection site, *J. Geophys. Res.*, *108*(A10), 1357, doi:10.1029/2003JA009900.
- Nakamura, R., et al. (2002), Fast flow during current sheet thinning, *Geophys. Res. Lett.*, *29*(23), 2140, doi:10.1029/2002GL016200.
- Nosé, M., A. T. Y. Lui, S. Ohtani, B. H. Mauk, R. W. McEntire, D. J. Williams, T. Mukai, and K. Yumoto (2000), Acceleration of oxygen ions of ionospheric origin in the near-Earth magnetotail during substorms, *J. Geophys. Res.*, *105*, 7669, doi:10.1029/1999JA000318.
- Nosé, M., S. Ohtani, K. Takahashi, A. T. Y. Lui, R. W. McEntire, D. J. Williams, S. P. Christon, and K. Yumoto (2001), Ion composition of the near-Earth plasma sheet in storm and quiet intervals: Geotail/EPIC measurements, *J. Geophys. Res.*, *106*, 8391, doi:10.1029/2000JA000376.
- Ogino, T. (1986), A three-dimensional MHD simulation of the interaction of the solar wind with the Earth's magnetosphere: The generation of field-aligned currents, *J. Geophys. Res.*, *91*, 6791, doi:10.1029/JA091iA06p06791.
- Ohtani, S., K. Takahashi, L. J. Zanetti, T. A. Potemra, R. W. McEntire, and T. Iijima (1992), Initial signatures of magnetic field and energetic particle fluxes at tail reconfiguration: Explosive growth phase, *J. Geophys. Res.*, *97*, 19,311, doi:10.1029/92JA01832.
- Papitashvili, V. O., F. Christiansen, and T. Neubert (2002), A new model of field-aligned currents derived from high-precision satellite magnetic field data, *Geophys. Res. Lett.*, *29*(14), 1683, doi:10.1029/2001GL014207.
- Paty, C., and R. Winglee (2004), Multi-fluid simulations of Ganymede's magnetosphere, *Geophys. Res. Lett.*, *31*, L24806, doi:10.1029/2004GL021220.
- Paty, C., and R. Winglee (2006), The role of ion cyclotron motion at Ganymede: Magnetic field morphology and magnetospheric dynamics, *Geophys. Res. Lett.*, *33*, L10106, doi:10.1029/2005GL025273.
- Potemra, T. A., L. J. Zanetti, R. E. Erlandson, G. Gustafsson, and M. H. Acuna (1988), First VIKING results: Magnetic field measurements, *Phys. Scr.*, *37*, 479, doi:10.1088/0031-8949/37/3/034.
- Reeves, G. D., R. W. H. Friedel, M. G. Henderson, A. Korth, P. S. McLachlan, and R. D. Belian (1996), Radial propagation of substorm injections, in *Substorms 3*, edited by E. J. Rolfe and B. Kaldeich, *Eur. Space Agency Spec. Publ., ESA-SP 389*, 579.
- Runov, A., R. Nakamura, W. Baumjohann, T. L. Zhang, M. Volwerk, H.-U. Eichelberger, and A. Balogh (2003), Cluster observation of a bifurcated current sheet, *Geophys. Res. Lett.*, *30*(2), 1036, doi:10.1029/2002GL016136.
- Runov, A., R. Nakamura, and W. Baumjohann (2006), Multi-point study of the magnetotail current, *Adv. Space Res.*, *38*, 85, doi:10.1016/j.asr.2004.09.024.
- Shiokawa, K., W. Baumjohann, and G. Haerendel (1997), Braking of high-speed flows in the near-Earth tail, *Geophys. Res. Lett.*, *24*, 1179, doi:10.1029/97GL01062.
- Sibeck, D. G., G. L. Siscoe, J. A. Slavin, E. J. Smith, S. J. Bame, and F. L. Scarf (1984), Magnetotail flux ropes, *Geophys. Res. Lett.*, *11*, 1090, doi:10.1029/GL011i010p01090.
- Sibeck, D. G., R. P. Lepping, and A. J. Lazarus (1990), Magnetic field line draping in the plasma depletion layer, *J. Geophys. Res.*, *95*, 2433, doi:10.1029/JA095iA03p02433.
- Slavin, J. A., et al. (1989), CDAW 8 observations of plasmoid signatures in the geomagnetic tail: An assessment, *J. Geophys. Res.*, *94*, 15,153, doi:10.1029/JA094iA11p15153.
- Slavin, J. A., C. J. Owen, M. M. Kuznetsova, and M. Hesse (1995), ISEE 3 observations of plasmoids with flux rope magnetic topologies, *Geophys. Res. Lett.*, *22*, 2061, doi:10.1029/95GL01977.
- Slavin, J. A., R. P. Lepping, J. Gjerloev, D. H. Fairfield, M. Hesse, C. J. Owen, M. B. Moldwin, T. Nagai, A. Ieda, and T. Mukai (2003a), Geotail observations of magnetic flux ropes in the plasma sheet, *J. Geophys. Res.*, *108*(A1), 1015, doi:10.1029/2002JA009557.
- Slavin, J. A., et al. (2003b), Cluster electric current density measurements within a magnetic flux rope in the plasma sheet, *Geophys. Res. Lett.*, *30*(7), 1362, doi:10.1029/2002GL016411.
- Slinker, S. P., J. A. Fedder, and J. G. Lyon (1995), Plasmoid formation and evolution in a numerical simulation of a substorm, *Geophys. Res. Lett.*, *22*, 859.
- Takada, T., et al. (2008), Plasma sheet oscillations and their relation to substorm development: Cluster and double star TC1 case study, *Adv. Space Res.*, *41*, 1585, doi:10.1016/j.asr.2007.04.008.
- Volwerk, M., K.-H. Glassmeier, A. Runov, W. Baumjohann, R. Nakamura, T. L. Zhang, B. Klecker, A. Balogh, and H. Rème (2003), Kink mode oscillation of the current sheet, *Geophys. Res. Lett.*, *30*(6), 1320, doi:10.1029/2002GL016467.
- Winglee, R. M. (1994), Non-MHD influences on the magnetospheric current system, *J. Geophys. Res.*, *99*, 13,437.
- Winglee, R. M. (1998), Multi-fluid simulations of the magnetosphere: The identification of the geopause and its variation with IMF, *Geophys. Res. Lett.*, *25*, 4441, doi:10.1029/1998GL900217.
- Winglee, R. M. (2000), Mapping of ionospheric outflows into the magnetosphere for varying IMF conditions, *J. Atmos. Sol. Terr. Phys.*, *62*, 527, doi:10.1016/S1364-6826(00)00015-8.
- Winglee, R. M. (2003), Circulation of ionospheric and solar wind particle populations during extended southward interplanetary magnetic field, *J. Geophys. Res.*, *108*(A10), 1385, doi:10.1029/2002JA009819.
- Winglee, R. M. (2004), Ion cyclotron and heavy ion effects on reconnection in a global magnetotail, *J. Geophys. Res.*, *109*, A09206, doi:10.1029/2004JA010385.
- Winglee, R. M., S. Kokubun, R. P. Lin, and R. P. Lepping (1998), Flux rope structures in the magnetotail: Comparison between Wind/Geotail observations and global simulations, *J. Geophys. Res.*, *103*, 135, doi:10.1029/97JA02415.
- Winglee, R. M., D. Chua, M. Brittacher, G. K. Parks, and G. Lu (2002), Global impact of ionospheric outflows on the dynamics of the magnetosphere and cross-polar cap potential, *J. Geophys. Res.*, *107*(A9), 1237, doi:10.1029/2001JA000214.
- Winglee, R. M., W. Lewis, and G. Lu (2005), Mapping of the heavy ion outflows as seen by IMAGE and multifluid global modeling for the 17 April 2002 storm, *J. Geophys. Res.*, *110*, A12S24, doi:10.1029/2004JA010909.
- Winglee, R. M., E. Harnett, A. Stickle, and J. Porter (2008a), Multiscale/multifluid simulations of flux ropes at the magnetopause within a global magnetospheric model, *J. Geophys. Res.*, *113*, A02209, doi:10.1029/2007JA012653.
- Winglee, R. M., W. K. Peterson, A. W. Yau, E. Harnett, and A. Stickle (2008b), Model/data comparisons of ionospheric outflow as a function of invariant latitude and magnetic local time, *J. Geophys. Res.*, *113*, A06220, doi:10.1029/2007JA012817.
- Zong, Q.-G., et al. (2004), Cluster observations of earthward flowing plasmoid in the tail, *Geophys. Res. Lett.*, *31*, L18803, doi:10.1029/2004GL020692.

E. Harnett, A. Kidder, and R. M. Winglee, Department of Earth and Space Sciences, University of Washington, Seattle, WA 98195-1310, USA. (winglee@ess.washington.edu)